UC Riverside
UC Riverside Previously Published Works

Title

Metallic Active Sites on MoO2(110) Surface to Catalyze Advanced Oxidation Processes for Efficient Pollutant Removal

Permalink

Journal

ISSN

Authors

Ji, Jiahui

Aleisa, Rashed M

Duan, Huan

et al.

Publication Date

DOI

Copyright Information

Peer reviewed

Article

Metallic Active Sites on MoO$_2$(110) Surface to Catalyze Advanced Oxidation Processes for Efficient Pollutant Removal
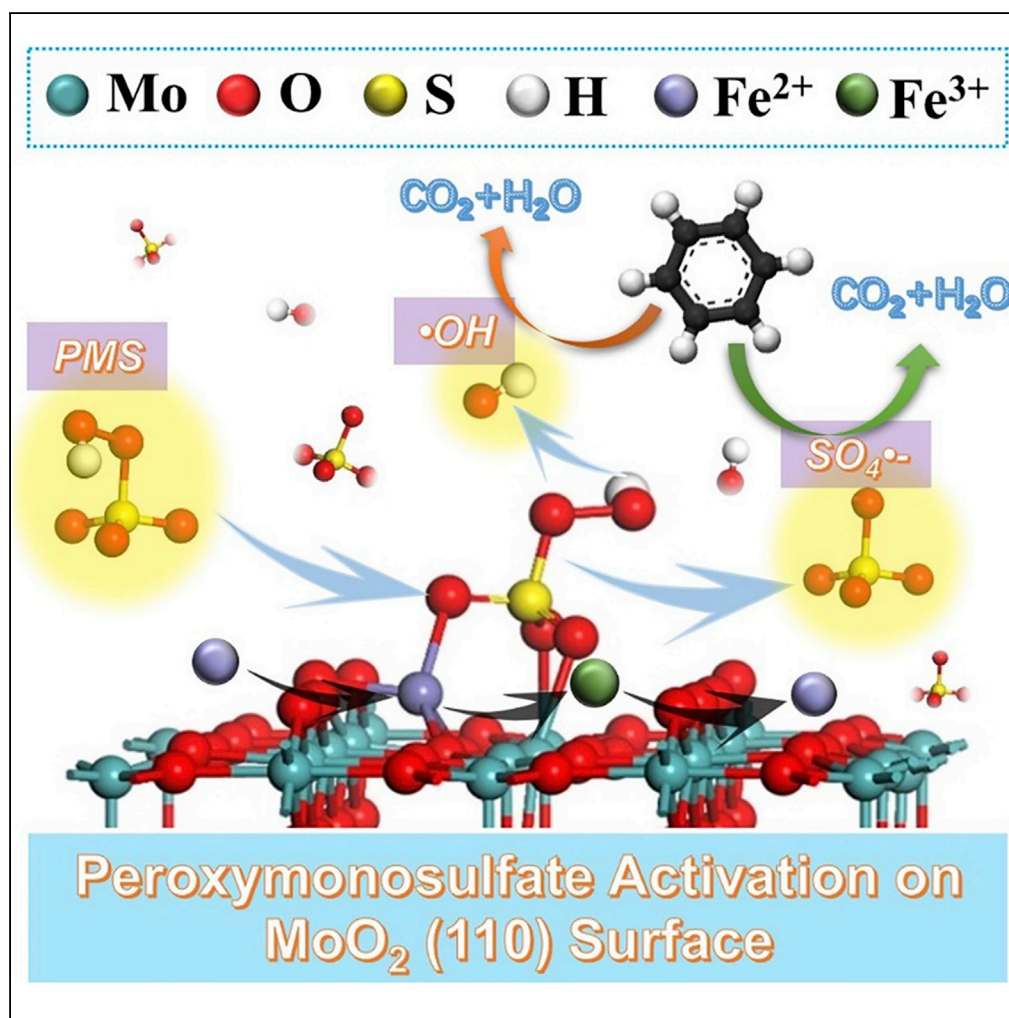
Jiahui Ji, Rashed M. Aleisa, Huan Duan, Jinlong Zhang, Yadong Yin, Mingyang Xing

mingyangxing@ecust.edu.cn

HIGHLIGHTS

The degradation rate of PMS/Fe(II)/MoO$_2$ system is 50 times higher than that without MoO$_2$

Fe(III)/Fe(II) cycle on (110) surface of MoO$_2$ in PMS/Fe(II)/MoO$_2$ system was confirmed

The metal active sites exposed to MoO$_2$ (110) surface are responsible for PMS activation

Compared with MoS$_2$, MoO$_2$ co-catalytic system has less toxicity and no release of H$_2$S

Article

Metallic Active Sites on MoO$_2$(110) Surface to Catalyze Advanced Oxidation Processes for Efficient Pollutant Removal

Jiahui Ji,[1] Rashed M. Aleisa,[2] Huan Duan,[3] Jinlong Zhang,[1] Yadong Yin,[2] and Mingyang Xing[1,4,*]
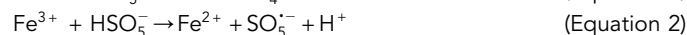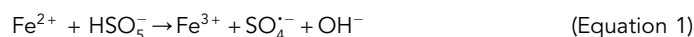
SUMMARY

Advanced oxidation processes (AOPs) based on sulfate radicals (SO$_4$$^{\bullet-}$) suffer from low conversion rate of Fe(III) to Fe(II) and produce a large amount of iron sludge as waste. Herein, we show that by using MoO$_2$ as a cocatalyst, the rate of Fe(III)/Fe(II) cycling in PMS system accelerated significantly, with a reaction rate constant 50 times that of PMS/Fe(II) system. Our results showed outstanding removal efficiency (96%) of L-RhB in 10 min with extremely low concentration of Fe(II) (0.036 mM), outperforming most reported SO$_4$$^{\bullet-}$-based AOPs systems. Surface chemical analysis combined with density functional theory (DFT) calculation demonstrated that both Fe(III)/Fe(II) cycling and PMS activation occurred on the (110) crystal plane of MoO$_2$, whereas the exposed active sites of Mo(IV) on MoO$_2$ surface were responsible for accelerating PMS activation. Considering its performance, and non-toxicity, using MoO$_2$ as a cocatalyst is a promising technique for large-scale practical environmental remediation.

INTRODUCTION

The presence of organic pollutants such as aromatic organic compounds in the environment is among the most significant issue for humans that requires immediate remediation (Muthuraman and Teng, 2009; Crini, 2006; Al-Ghouti et al., 2003). These pollutants are toxic, carcinogenic, and recalcitrant to degrade with time, demonstrating the great need for their removal (Ito et al., 2016; Du et al., 2018b; Yi et al., 2015; Dong et al., 2018). Although several processing methods have been proposed for effectively removing organic compounds from places such as drinking water, advanced oxidation processes (AOPs) based on the generation of hydroxyl radicals ($^\bullet$OH) are among the most promising techniques because they are inexpensive, environmentally safe (Buck et al., 2018; Yang et al., 2019, Tao et al., 2001), and efficient in oxidizing almost all organic pollutants to harmless products (Clarizia et al., 2017).

Recently, sulfate radical (SO$_4$$^{\bullet-}$)-based AOPs have drawn much interests (Zhang et al., 2016; Yun et al., 2018; Chen et al., 2018) due to their higher oxidation potentials (SO$_4$$^{\bullet-}$, 2.5–3.1 eV) compared with hydroxyl radical ($^\bullet$OH, 2.8 eV), longer half-life, higher selectivity (Li et al., 2018; Huang et al., 2017; Hu et al., 2017), and tolerance to wider pH range (2–8) (Ghanbari and Moradi, 2017). Peroxymonosulfate (PMS) molecules are widely used as a source for sulfate radicals in AOPs, which can be activated during the treatment process through various methods such as heating (Chen et al., 2016), UV light (Guan et al., 2011), transition metal ions, and ultrasound (Liu et al., 2017; Du et al., 2018a). Dionysiou et al. found that PMS can be activated by various transition metals, among which Co(II) and Ru(III) demonstrated the best performances as catalysts for generating sulfate radicals (Anipsitakis and Dionysiou, 2003, 2004). However, their high toxicity and scarcity significantly limited their implementation in PMS activation system. A more environmental and economical alternative to Co and Ru has been found to be Fe(II), which can decompose PMS and generate SO$_4$$^{\bullet-}$ in a similar manner (Dan et al., 2014). Generally, the stoichiometric ratio of PMS to Fe(II) is maintained at approximately 1:1 according to Equation 1. Transformation from Fe(III) to Fe(II) was found to be the limiting step for the reaction (Anipsitakis and Dionysiou, 2003). Besides, the activation of PMS by Fe(III) will also produce SO$_5$$^{\bullet-}$ (1.1 eV) under acidic conditions (Equation 2), greatly decreasing its oxidation capacity (Anipsitakis and Dionysiou, 2004).

$$Fe^{2+} + HSO_5^- \rightarrow Fe^{3+} + SO_4^{\bullet-} + OH^- \qquad \text{(Equation 1)}$$
$$Fe^{3+} + HSO_5^- \rightarrow Fe^{2+} + SO_5^{\bullet-} + H^+ \qquad \text{(Equation 2)}$$

In addition, the amount required for Fe(II) to be used in PMS activation is considered extremely large, which is also responsible for producing large amount of iron sludge (Rastogi et al., 2009b). Therefore, several

[1]Key Laboratory for Advanced Materials and Joint International Research Laboratory of Precision Chemistry and Molecular Engineering, Feringa Nobel Prize Scientist Joint Research Center, School of Chemistry and Molecular Engineering, East China University of Science and Technology, 130 Meilong Road, Shanghai 200237, China

[2]Department of Chemistry, University of California, Riverside, Riverside, CA 92521, USA

[3]School of Chemistry and Chemical Engineering, Southwest University, Chongqing 400715, China

[4]Lead Contact

*Correspondence: mingyangxing@ecust.edu.cn

https://doi.org/10.1016/j.isci.2020.100861

other combination methods have been proposed to further enhance the performance of Fe(II) in PMS activation system. For example, iron tetracarboxyphthalocyanine molecules were synthesized as a homogeneous catalyst to activate PMS, which outperformed the performance of Co(II) (Dai et al., 2017). Also, a p-Mn/Fe$_3$O$_4$ catalyst with high porosity showed excellent regeneration ability just by simply washing with deionized water (Du et al., 2018a). Assisted UV irradiation has shown also to greatly improve the regeneration of Fe(II) (Khan et al., 2016). However, the following factors need to be considered when using the assisted-Fe(II)/PMS activation: (1) the elimination of competitive reaction between organic complexes and pollutants; (2) the reduction of energy consumption during the process; and (3) the simplicity of preparation and availability of the assisted materials or methods. Recently, AOPs with MoS$_2$ as a cocatalyst have achieved surprising results (Xing et al., 2018; Wang et al., 2020; Sheng et al., 2019). However, there are still some critical problems with MoS$_2$ as a cocatalyst to decompose PMS: the inevitable secondary pollution caused by the generation of H$_2$S during reaction and the fact that MoS$_2$ itself can activate PMS, leading to itself to be consumed.

Therefore, there is an urgent need to develop a greener and more efficient cocatalyst that can replace MoS$_2$ for rapid, stable, and efficient cocatalytic decomposition of PMS for environmental remediation. Here, we present a facile strategy to significantly enhance the performance of SO$_4^{\bullet-}$-based AOPs by using molybdenum dioxide (MoO$_2$) as a cocatalyst in PMS/Fe(II) system. The oxidation efficiencies of PMS/Fe(II)/MoO$_2$ system were examined with different aromatic organic pollutants, including lissaminerhodamine B (L-RhB), phenol, methylene blue (MB), sulfadiazine, and norfloxacin. Among them, the degradation rate of L-RhB in the PMS/Fe(II)/MoO$_2$ system was significantly improved, 50 times higher than that in the PMS/Fe(II) system, with removal efficiency of 96% in 10 min while very low concentration of Fe(II) was used (0.036 mM), exceeding most reported PMS/Fe(II) systems. We further employed surface chemical analysis and DFT calculation to understand the cocatalytic enhancement of MoO$_2$. The results revealed that the (110) crystal plane of MoO$_2$ worked as active site for PMS activation, where the exposed Mo(IV) on the MoO$_2$ cocatalyzed the conversion of Fe(III) to Fe(II). To the best of our knowledge, this is the first report of utilization MoO$_2$ as a cocatalyst in SO$_4^{\bullet-}$-based AOPs. Compared with MoS$_2$ cocatalytic AOPs system, MoO$_2$ cocatalytic system has higher valence band free electron density, less toxicity, better stability, and no release of secondary pollutants H$_2$S (Hu et al., 2009). Therefore, it is reasonable to believe that MoO$_2$ cocatalytic activation of PMS will have greater potential for large-scale practical environmental remediation.

RESULTS

MoO$_2$ Cocatalytic PMS/Fe(II) System for the Oxidation Reaction

As shown in Figure 1A, no oxidation of L-RhB was observed in the absence of PMS. Besides, in the absence of Fe(II) ions, the oxidation efficiency was extremely low that only 4.1% of L-RhB was removed. This is attributed mainly to almost no production of reactive radical species in the absence of PMS or Fe(II). When the concentration of Fe(II) was fairly low (0.036 mM) and no MoO$_2$ was added, the degradation performance of the PMS/Fe(II) system remained poor because of the slow conversion rate of Fe(III) to Fe(II) (Anipsitakis and Dionysiou, 2004), with only 29% of L-RhB degraded within 30 min. However, when all components were involved, L-RhB degraded near completely in 10 min (96%), indicating that MoO$_2$ accelerated the conversion from Fe(III) to Fe(II), leading to continuous activation of PMS.

We also found that the degradation rate slowed as the concentration of L-RhB increased (Figure 1B), because there is always a constant number of radical species generated when the amount of PMS is fixed. In addition to L-RhB, the PMS/Fe(II)/MoO$_2$ system also showed a rapid and effective degradation of other organic pollutants. Figure 1C shows that phenol, MB, sulfadiazine, and norfloxacin were degraded by 69%, 84%, 80%, and 59% in 30 min, respectively, demonstrating the potentials of this system for remediating various organic pollutants.

To explore the influence of MoO$_2$, Fe(II), and PMS concentrations on the reaction rate, a series of experiments were conducted to determine the best reaction conditions (Figures S1A–S1C). The oxidation rate of L-RhB becomes faster with the increase of Fe(II) and MoO$_2$ at pH 3.0 (Figures S1A and S1B). It is worth noting that the concentration of Fe(II) in the solution was extremely low (0–0.036 mM), far less than the molar amount of PMS, so the increase of Fe(II) concentration had a significant effect on the PMS activation (Anipsitakis and Dionysiou, 2003). The more addition of MoO$_2$ provided more redox active sites for the transformation from Fe(III) to Fe(II), resulting in the rapid oxidation of L-RhB. However, with the increase of PMS (Figure S1C), the degradation rate first increased and then decreased a little, reaching the
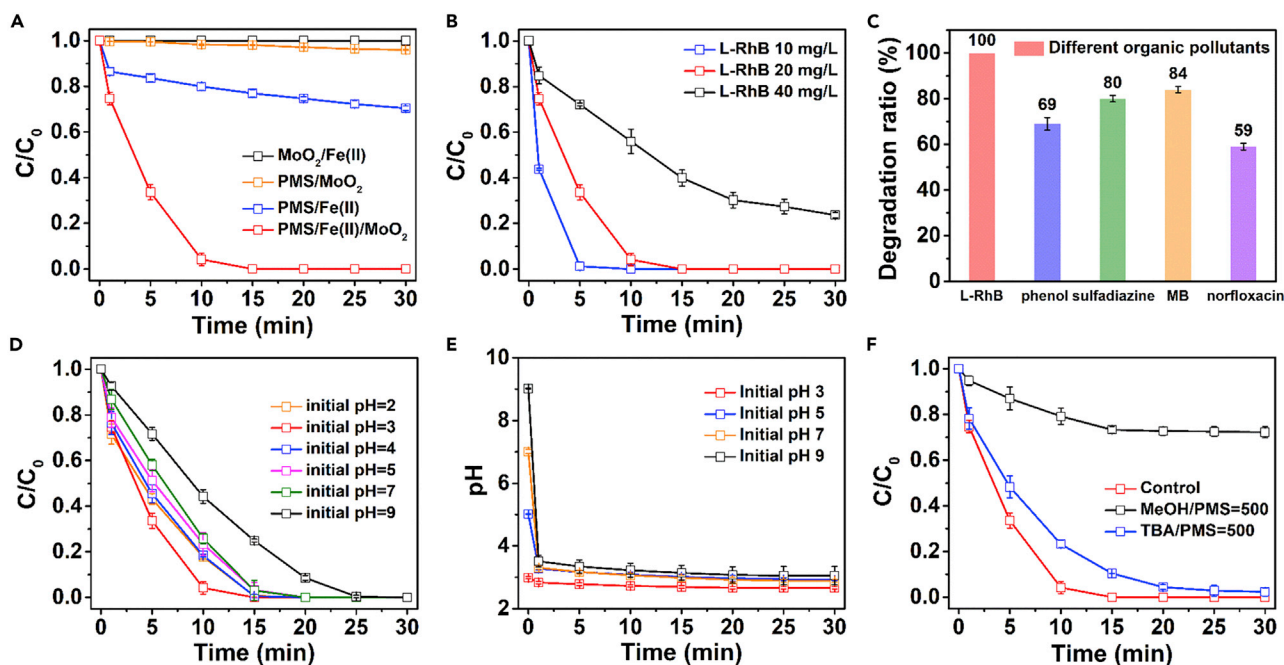
Figure 1. Exploration of the Best Reaction Conditions for PMS/Fe(II)/MoO$_2$ System

(A) Oxidation of L-RhB in different systems; oxidation of different (B) L-RhB concentrations; (C) organic compounds in the PMS/Fe(II)/MoO$_2$ system; (D) the effect of initial pH and (E) variation of pH on L-RhB degradation in the PMS/Fe(II)/MoO$_2$ system; (F) inhibition effect of radical scavengers on L-RhB degradation in the PMS/Fe(II)/MoO$_2$ system. General conditions: [PMS]$_0$ = 0.650 mM, [Fe(II)]$_0$ = 0.036 mM, [MoO$_2$]$_0$ = 300 mg/L, initial pH = 3.0, [organic compound]$_0$ = 20 mg/L. Error bars represent the standard deviation from at least duplicate experiments.

maximum when the adding amount of PMS was 0.650 mM, which could be attributed to the scavenging of SO$_4^{\bullet-}$ by excess PMS to produce SO$_5^{\bullet-}$ (1.1 eV) via Equation 3 (Ling et al., 2010).

$$SO_4^{\bullet-} + HSO_5^- \rightarrow SO_4^{2-} + SO_5^{\bullet-} + H^+ \qquad \text{(Equation 3)}$$
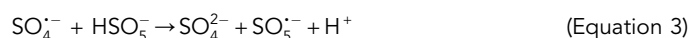
The kinetics were investigated by using a first-order kinetic model, as in the following equation: $-\ln(C/C_0) = k \cdot t$, where C_0 and C represent organic matter concentrations at time $t = 0$ and t, respectively, and k (min^{-1}) is the reaction rate constant (Figures S1D–S1F). Figures S1D–S1F show that the experiment results were fitting the first-order kinetics well. Not surprisingly, the reaction rate constant (k) was upgraded with the increase of Fe(II) and MoO$_2$. Specifically, the k value with the condition of 0.036 mMFe(II) (0.311 min^{-1}) was 222 times faster than that without Fe(II) (0.00140 min^{-1}). Meanwhile, the addition of MoO$_2$ made "k" 4–50 times faster than that with no MoO$_2$ added (0.00938 min^{-1}), and there was no striking difference between 300 mg/L and 600 mg/L MoO$_2$ added. When the PMS concentration was 0.650 mM, the k value was the largest, about 2.3 times higher than that with 0.325 mM and a little higher than that with 1.300 mM. As a result, we concluded that Fe(II) had the greatest influence on the reaction rate in the PMS/Fe(II)/MoO$_2$ system, whereas the addition of MoO$_2$ significantly reduced the required amount of Fe(II), and the amount of PMS greatly determined the amount of radical species generated.
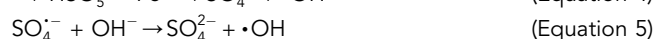
In the exploration of the influence of the initial pH in the mixture, we found that L-RhB could be removed efficiently in 30 min with a wide initial pH range of 2.0–9.0, as shown in Figure 1D. An increase in the degradation efficiency of L-RhB was obtained by increasing the initial pH from 2.0 to 3.0, in which Fe(OH)$_2$ might form and activate PMS more efficiently as reported previously (Pignatello et al., 2006). However, L-RhB could be still completely oxidized within 20 min when the initial pH was neutral. There was a slight decrease in the degradation rate when the initial pH increased from 4.0 to 7.0. It has been reported that Fe(II) coprecipitates with Fe(III) oxyhydroxides when both Fe(II) and Fe(III) coexist under a pH value over 3.0. The degradation rate of L-RhB continued to decrease as the initial pH was increased to 9.0 because of more iron coprecipitation. Thus, the fastest degradation rate was obtained at pH 3.0. According to Equation 1, when Fe(II) activates PMS, OH$^-$ is generated. Under acidic conditions, the generated OH$^-$ can be quickly neutralized so that the reaction can proceed in the positive reaction direction. Moreover, under acidic conditions,

Fe(II) is not easily complexed with OH^-, which leads its precipitation. Thus, PMS can be activated more easily by Fe(II) under acidic conditions. Nevertheless, with the increase in initial pH, the removal efficiency of L-RhB in the PMS/Fe(II)/MoO$_2$ system varied slightly but remained superior compared with the PMS/Fe(II) system. The variation of pH values in the system was also measured during the reaction process as shown in Figure 1E. Considering the possibility of radical consumption or complexation with Fe(II) or Fe(III), there were no buffering reagents included in the solution so far. Regardless of the initial pH of the system, the reaction solution would quickly become acidic when PMS was added, because KHSO$_4$ molecules are essential part of the PMS mixtures (Wacławek et al., 2015). Also, the pH values slowly declined until PMS was completely consumed (Figure 1E). This explains why the PMS/Fe(II)/MoO$_2$ system maintained a high level of activity in the treatment of neutral dye solution because this dropping of pH value would suppress the precipitation of Fe(II), keeping Fe(II) at high catalytic activity in the acidic solution. Moreover, the influence of solution pH was also investigated with potassium hydrogen phthalate ($C_8H_5KO_4$, pH 4.00), mixed phosphate (pH 6.86), and borax ($Na_2B_4O_7 \cdot 10H_2O$, pH 9.18) buffer solutions, respectively. As shown in Figure S2, the degradation efficiency of L-RhB became extremely poor at all three different pH conditions, which may be attributed to the consumption of most of the free radicals by the ions in the buffer solution, leading to few free radicals attacking L-RhB molecular (Zou et al., 2013).

We concluded that the optimal conditions for the degradation of L-RhB were as follows: an initial pH value of 3.0, PMS concentration of around 0.650 mM, and the more MoO$_2$ and Fe(II) are added to the system, the faster the reaction rate will be. Given that moderate dosages of 300 mg/L MoO$_2$ and 0.036 mM Fe(II) were enough to completely degrade L-RhB, they were chosen for most further experiments in the subsequent investigations. Ultimately, the performance of PMS/Fe(II)/MoO$_2$ system was also compared with other reported heterogeneous catalysis $SO_4^{\bullet-}$-based AOPs, where its removal efficiency performed most reported values as shown in Table S1.

Identification of Reactive Species in the PMS/Fe(II)/MoO$_2$ System

KHSO$_5$ has an asymmetric structure ($HO-O-SO_3^-$), so it can be activated to produce sulfate radical ($SO_4^{\bullet-}$) via Equation 1, persulfate radical ($SO_5^{\bullet-}$) via Equation 2, or hydroxyl radicals ($^\bullet OH$) via Equation 4. At the same time, those radicals interconvert via Equations 5 and 6, which is partially influenced by the solution pH (Duan et al., 2018). For further exploration of the main reactive species throughout the organic oxidation process, selective radical quenching tests were done with TBA and MeOH. The carbon atom of MeOH attached to the hydroxyl has three α-hydrogens [$(\alpha$-H)$_3$-C-OH], which allows methanol to capture $^\bullet OH$ ($k = (1.2-2.8) \times 10^9 \, M^{-1} \cdot s^{-1}$) and $SO_4^{\bullet-}$ ($k = (1.6-7.7) \times 10^7 \, M^{-1} \cdot s^{-1}$)] at high reaction rates. On the other hand, TBA, which has no α-hydrogen, can react with $^\bullet OH$ ($k = (3.8-7.6) \times 10^8 \, M^{-1} \cdot s^{-1}$) faster than $SO_4^{\bullet-}$ ($k = (4.0-9.1) \times 10^5 \, M^{-1} \cdot s^{-1}$) (Liang and Su, 2009). However, both MeOH and TBA are nonreactive with $SO_5^{\bullet-}$ ($k \leq 10^3 \, M^{-1} \cdot s^{-1}$) (Hayon et al., 1972). Therefore, the contributions of $SO_5^{\bullet-}$ and $^\bullet OH/SO_4^{\bullet-}$ can be differentiated by MeOH, whereas TBA can be employed to distinguish the contributions of $^\bullet OH$ and $SO_4^{\bullet-}$.

$$Fe^{2+} + HSO_5^- \rightarrow Fe^{3+} + SO_4^{2-} + \cdot OH \qquad \text{(Equation 4)}$$

$$SO_4^{\bullet-} + OH^- \rightarrow SO_4^{2-} + \cdot OH \qquad \text{(Equation 5)}$$

$$HSO_4^- + \cdot OH \rightarrow SO_4^{\bullet-} + H_2O \qquad \text{(Equation 6)}$$

As shown in Figure 1F, when the molar ratio of MeOH to PMS was maintained as 500:1, only 26% of L-RhB was degraded, which confirms the small contribution of $SO_5^{\bullet-}$ in the system. However, 100% degradation efficiency was achieved in 30 min when 500 times molar ratio of TBA to PMS was maintained in the mixture, which was much slower compared with the controlled experiment. This result indicates that the radicals generated from PMS were mainly $SO_4^{\bullet-}$, $^\bullet OH$, and a small number of $SO_5^{\bullet-}$. The presence of Fe(II) under acidic conditions implies that $SO_4^{\bullet-}$ and $^\bullet OH$ contributed the most to L-RhB degradation. To further prove the generation of $^\bullet OH$, the photoluminescence (PL) signal of hydroxybenzoic acid formed by benzoic acid capturing $^\bullet OH$ was measured. As shown in Figure 2A, the signal of hydroxybenzoic acid increased significantly in the first five minutes and then slowed down, which is consistent with the interpretation that $^\bullet OH$ plays a significant role in the system.

To further support these assumptions, electron paramagnetic resonance (EPR) was employed to detect the existence of radicals, coupled with 5,5-dimethyl-1-pyrroline (DMPO) as a spin-trapping reagent that can capture both $SO_4^{\bullet-}$ and $^\bullet OH$. The intensity of DMPO radical adducts is in direct proportion to the concentration of reactive radical species (Zamora and Villamena, 2012; Fang et al., 2017). As illustrated in Figure 2B,
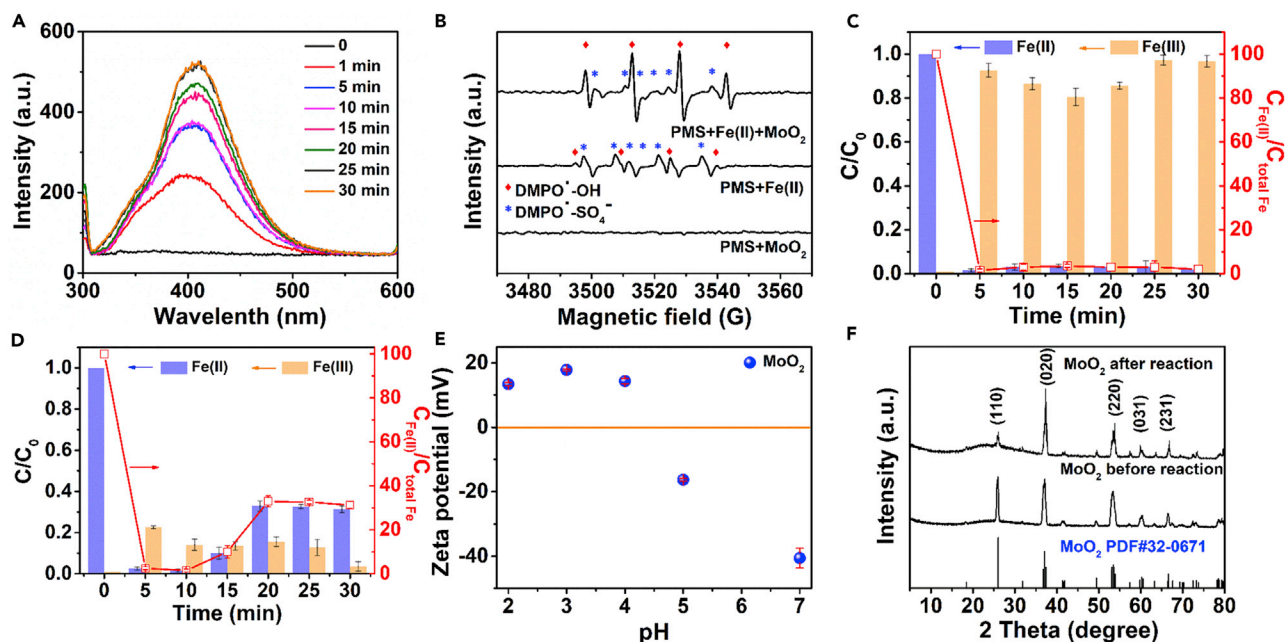
Figure 2. Exploration of Reactive Species and Reaction Mechanism

(A) Photoluminescence spectra of benzoic acid mixed with the PMS/Fe(II)/MoO$_2$ system; (B) EPR spectra obtained from the PMS/MoO$_2$ system, PMS/Fe(II) system, and PMS/Fe(II)/MoO$_2$ system with the existence of DMPO (♦ represents DMPO·-OH adduct and * represents DMPO·-SO$_4^-$ adduct); the variation of Fe(II) and Fe(III) concentrations in (C) the PMS/Fe(II) system; (D) the PMS/Fe(II)/MoO$_2$ system; (E) zeta potential of MoO$_2$ at different pH values; (F) XRD patterns of MoO$_2$ before and after the reaction. General conditions: [PMS]$_0$ = 0.650 mM, [Fe(II)]$_0$ = 0.036 mM (total Fe), [MoO$_2$]$_0$ = 300 mg/L, initial pH = 3.0, [L-RhB]$_0$ = 20 mg/L. Error bars represent the standard deviation from at least duplicate experiments.

compared with the low EPR signals in the PMS/Fe(II) system and no EPR signal in the PMS/MoO$_2$ system, the PMS/Fe(II)/MoO$_2$ system exhibited the characteristic DMPO·-OH and DMPO·-SO$_4^-$ adduct signals, which further indicates that both ·OH and SO$_4^{·-}$ were generated during PMS activation. The addition of MoO$_2$ only facilitated the recycle of Fe(III)/Fe(II), hence promoting the generation of radical species. Moreover, the intensity of DMPO·-SO$_4^-$ adduct signals was much lower than the DMPO·-OH adduct signals. This might be attributed to the fast conversion of DMPO·-SO$_4^-$ adducts to DMPO·-OH adducts through the nucleophilic substitution reaction (Furman et al., 2010, Timmins et al., 1999).

Exploration of PMS Activation Mechanism in PMS/Fe(II)/MoO$_2$ System

The slow conversion of Fe(III) to Fe(II) is the rate-determining step in effective PMS activation (Rastogi et al., 2009a, 2009b). Based on our results, the acceleration of L-RhB oxidation rate was attributed to MoO$_2$ promoting the transformation of Fe(III) to Fe(II), consequently leading to faster activation of PMS. To further explore this hypothesis, the valence levels of Fe(II) and Fe(III) during the reaction were investigated. According to Equation 4, the ratio of Fe(II) to Fe(III) is believed to be positively correlated with the activation rate of PMS. 1,10-phenanthroline molecule can complex with Fe(II) to produce the jacinth complex in a pH range of 2–9 (Harvey et al., 1955, Herrera et al., 1989), whereas potassium thiocyanate (KSCN) is usually used to coordinate with Fe(III) to produce a blood-red complex (Kusic et al., 2011). As shown in Figures 2C and 2D, before the addition of PMS, the concentrations of Fe(II) (blue bar) were the same, whereas no Fe(III) was detected in the solutions (orange bar) in both the PMS/Fe(II) system and the PMS/Fe(II)/MoO$_2$ system. When PMS was added, the concentrations of Fe(II) in the solutions rapidly decreased, and the concentrations of Fe(III) reached their maximum values within 5 min, illustrating that most Fe(II) was immediately oxidized to Fe(III) by PMS (Equation 1), and the reduction of Fe(III) was slow in the system (Equation 2). Fe(II) was extremely low during L-RhB oxidation in both systems. After almost complete consumption of PMS, Fe(III) was gradually reduced to Fe(II) by MoO$_2$ until it maintained a relative dynamic equilibrium with the residual PMS, further indicating that MoO$_2$ continuously accelerate the conversion of Fe(III) to Fe(II) because the presence of PMS made Fe(II) difficult to exist stably. After the PMS was almost consumed, the stable existence of Fe(II) could be detected. Notably, the equilibrium concentration of Fe(III) in the
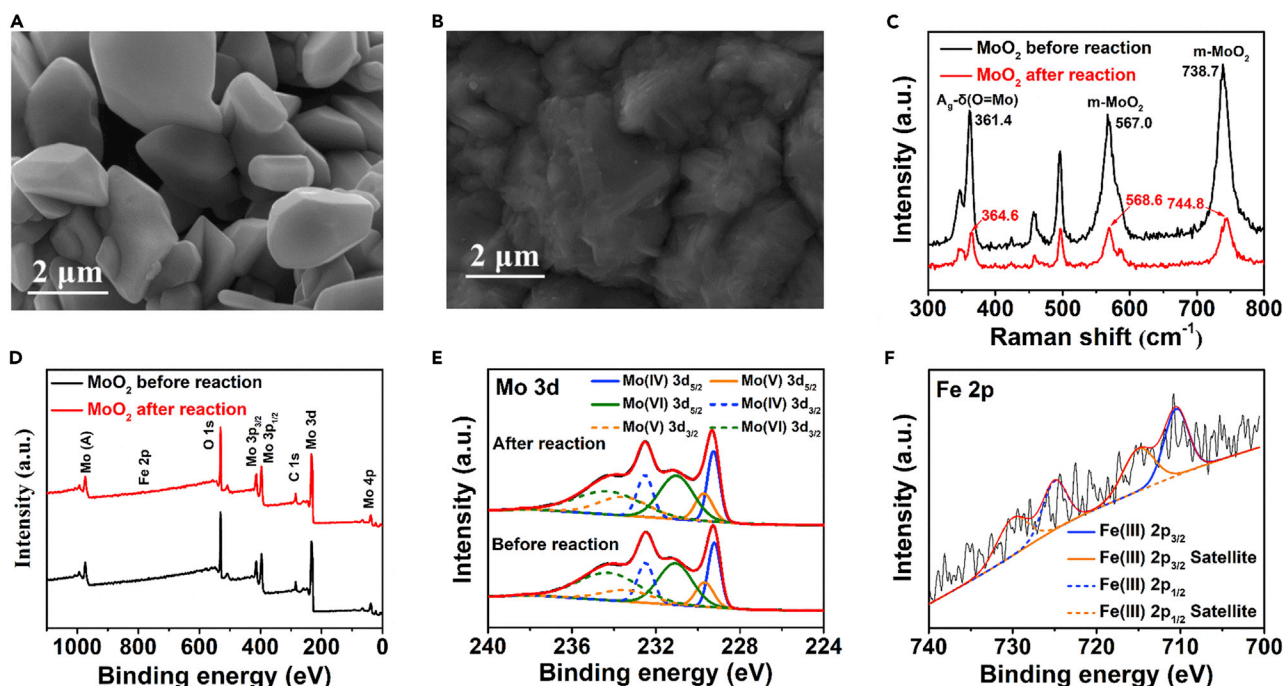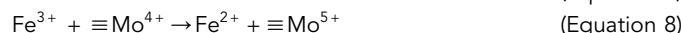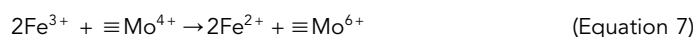
Figure 3. Characterization of MoO₂ before and after the Reaction

SEM images of MoO₂ (A) before and (B) after reaction; (C) Raman spectra of MoO₂ before and after reaction; (D) XPS survey spectra and (E) Mo3d spectra of MoO₂ before and after reaction; (F) Fe2p spectra of adsorbed iron after reaction in PMS/Fe(II)/MoO₂ system.

PMS/Fe(II)/MoO₂ system was much lower than that in the PMS/Fe(II) system. Therefore, zeta potential tests were conducted to determine the isoelectric point (IEP) of MoO₂. The results showed that its IEP was between pH 4 and 5 (Figure 2E). Because the pH was lower than 4 during the reaction, the surface of MoO₂ would be positively charged, leading PMS to be easily adsorbed, and then Fe(II) could be absorbed as well. Then, MoO₂ was recovered, dried, and redispersed in an acidic aqueous solution (pH = 3) after completing the oxidation reaction. Through ICP measurements of the supernatant, we found that the iron ions adsorbed on the surface of MoO₂ accounted for 87.7% of the initial amount, which could explain the low equilibrium concentration of Fe(III) and the incomplete recovery of Fe(II) in the PMS/Fe(II)/MoO₂ system.

$$2Fe^{3+} + \equiv Mo^{4+} \rightarrow 2Fe^{2+} + \equiv Mo^{6+} \qquad \text{(Equation 7)}$$

$$Fe^{3+} + \equiv Mo^{4+} \rightarrow Fe^{2+} + \equiv Mo^{5+} \qquad \text{(Equation 8)}$$

Given that the reduction potential of Fe(III)/Fe(II) (0.77 V) is higher than that of MoO_4^{2-}/MoO_2 (0.65 V) (Du et al., 2018a), it could be speculated that Mo(IV) on the surface of MoO₂ was oxidized by Fe(III) to Mo(V) and Mo(VI) (Equation 7). Fe(III) was converted to Fe(II) simultaneously (Equation 8), which was supported by Figure S3. (Ugo et al., 2002) To further support this argument, we studied the surface conditions of MoO₂ via SEM, XRD, Raman, and XPS, as depicted in Figures 2F and 3. Figures 3A and 3B display the SEM images of MoO₂ before and after reaction. It can be seen that the surface of MoO₂ after reaction was much rougher than that before the reaction, which proves that MoO₂ participated in the reaction. However, the XRD spectra in Figure 2F shows that the crystalline structure of MoO₂ did not change after the reaction, demonstrating that the deformed monoclinic structure of MoO₂ was quite stable, but the relative strength of the crystal plane (110) decreased, which might be ascribed to the redox reaction taking place on this plane and changing its surface condition (Xie et al., 2015, Sun et al., 2011). Moreover, the surface property of MoO₂ was investigated by Raman spectroscopy. The variety of electron cloud density causes red/blue shift of Raman peaks. As shown in Figure 3C, A$_g$-δ(O=Mo) peak and two m-MoO₂ peaks of MoO₂ are blue shifted by 3, 1, and 6 cm⁻¹, respectively, after reaction (Camacho-López et al., 2011), because the electron clouds on the surface of MoO₂ transfer to Fe(III), leading to the decrease of the probability of collision between photons and electrons, so that the average free path of collision increases and the energy loss caused by collision decreases. Therefore, the energy of photons scattered by MoO₂ after reaction is higher than that of the ones scattered by MoO₂ before reaction, causing the displacement

of three peaks of Raman spectra, the oxidation of Mo(IV), and the reduction of Fe(III). The variety of valence state of Mo in MoO_2 was evaluated by X-ray photoelectron spectroscopy (XPS). Five distinct peaks in the survey spectra of the MoO_2 before and after reaction are exhibited in Figure 3D, which can be indexed to Mo 3d (232.7 eV), C 1s (284.7 eV), Mo 3p (396.7 and 413.7 eV), and O 1s (530.7 eV), respectively. The Mo 3d peaks were further explored by high-resolution XPS. Figure 3E shows the multiple peak of Mo 3d spectra, which are fitted well into three spin-orbit doublets, coinciding to the peaks of Mo(IV), Mo(V), and Mo(VI) oxidation states. In detail, the two Mo 3d peaks of MoO_2 before/after reaction centered at 229.2/229.3 and 232.5/232.5 eV can be attributed to Mo(IV) $3d_{5/2}$ and Mo(IV) $3d_{3/2}$, the two peaks located at 229.7/229.7 and 233.4/233.5 eV are indexed to Mo(V) $3d_{5/2}$ and Mo(V) $3d_{3/2}$ (Zhang et al., 2019, Barros et al., 2003, Yi et al., 2019), and the other two peaks located at 231.1/231.0 and 234.3/234.3 eV are inferred to Mo(VI) $3d_{5/2}$ and Mo(VI) $3d_{3/2}$ (Camacho-López et al., 2011, Hanawa et al., 2001, Xie et al., 2015). Detailed fitting data are listed in Table S2 and the peak area ratios of Mo(IV)/(Mo(V)+Mo(VI)) are calculated, which varies from 0.355 to 0.346, manifesting that some of Mo(IV) on the sample surface was oxidized to Mo(V) and Mo(VI), leading to a slight decrease of the ratios. Fe ions (0.21 at.%) were also detected on the surface of MoO_2, which is consistent with the result of the ICP test, but it is difficult to split the peak of Fe2p high-resolution XPS due to the low content of Fe. As shown in Figure 3F, Fe(III) and its satellite peaks are fitted (Tang et al., 2015), proving the existence of Fe(III) on the surface of MoO_2. Moreover, as shown in Figure S4, almost no change was found between O1s spectra of MoO_2 before and after reaction (Xia et al., 2018), indicating that no iron oxide was formed.

DFT Calculation

DFT calculation was employed to investigate the reaction mechanism in the PMS/Fe(II)/MoO_2 system. MoO_2 has a monoclinic crystal structure, with P21c space group, and unit cell dimensions of a = 5.611 Å, b = 4.856 Å, c = 5.629 Å, and β = 120.95° (Brandt, 1971). Figure S5A shows its crystal structure, which consists of distorted octahedral [MoO_6] units. Structural optimizations of bulk MoO_2 were performed at a series of volumes to obtain the equilibrium unit cell parameters. The calculated lattice parameters (a = 5.594 Å, b = 4.910 Å, c = 5.682 Å) and bond angle (β = 120.47°) were generally consistent with experimental data. To better understand the activation mechanism of PMS molecules (labeled as HSO_5^- in Figure S5B) on the MoO_2 surfaces, DFT calculations were performed to determine which species are stable. The most commonly studied surface in rutile-type MoO_2 systems is the (110) plane, where the atomic layers along the [110] direction are ordered as MoO-O-O'-MoO (Tokarz-Sobieraj et al., 2011). The MoO_2 (110) surface possesses three distinct surface terminations: (1) both Mo and O atoms exposed, (2) with O atoms exposed, and (3) O' atoms exposed, as shown in Figures S5C–S5E. The comparison of surface formation energy—1.25 J/m^2, 1.12 J/m^2, and 0.79 J/m^2—indicated that a surface with the "bridging oxygen" termination (O' termination) was most likely to form, hence, it was selected for the further analysis.

As shown in Figure 4A, during the activation on the MoO_2 (110) surface, the PMS molecule was likely to locate at the MoO_2 (110) surface with the two O atoms on the -SO_4 side bonding with two Mo atoms of the surface. The two bond lengths were calculated as 2.09 Å and 2.07 Å, respectively. In addition, the H atom on the -OH side would form a hydrogen bond with the O' termination (approximately 1.80 Å in length), where the O-O bond length (l_{O-O}) rarely changed after its adsorption. All these inhibited the generation of hydroxyl radicals, which could explain the poor performance of MoO_2 alone in activating PMS. For the adsorption of PMS on the Fe(II)-decorated O' surface, the PMS attached to the surface with three O atoms from -SO_4 group binding the Fe(II) and two Mo atoms, as shown in Figure 4B. The bond lengths were calculated as 2.08 Å, 2.24 Å, and 2.27 Å, respectively. The adsorption between PMS and surface was enhanced by these three bonds, the occurrence of more electron transfer, and that -OH side would be maintained far from the surface, leading to an elongation of l_{O-O}. To better understand the interaction between the surfaces and PMS activation, we calculated the adsorption energy of PMS (E_{ads}) on the different surfaces, charge transfer (Δq) between PMS and (110) surfaces, and the bond length (l_{O-O}) between the -OH group and -SO_4 group. All results are summarized in Table S3. The adsorption on both surfaces was found to be strong, with E_{ads} being −2.06 and −3.17 eV for MoO_2 (110) surface without and with Fe(II) respectively. This was also consistent with the formation of chemical bonds between PMS and the two surfaces, illustrating the strong interaction between PMS and Fe(II) and electrons transferred from the surface atoms to the PMS molecules. The adsorption of PMS on Fe(II)-(110) was stronger, with lower E_{ads}, longer l_{O-O}, and more electrons received from the metal atoms on the surface. Therefore, we concluded that the PMS on the modified MoO_2 (110) surface was the most active site.
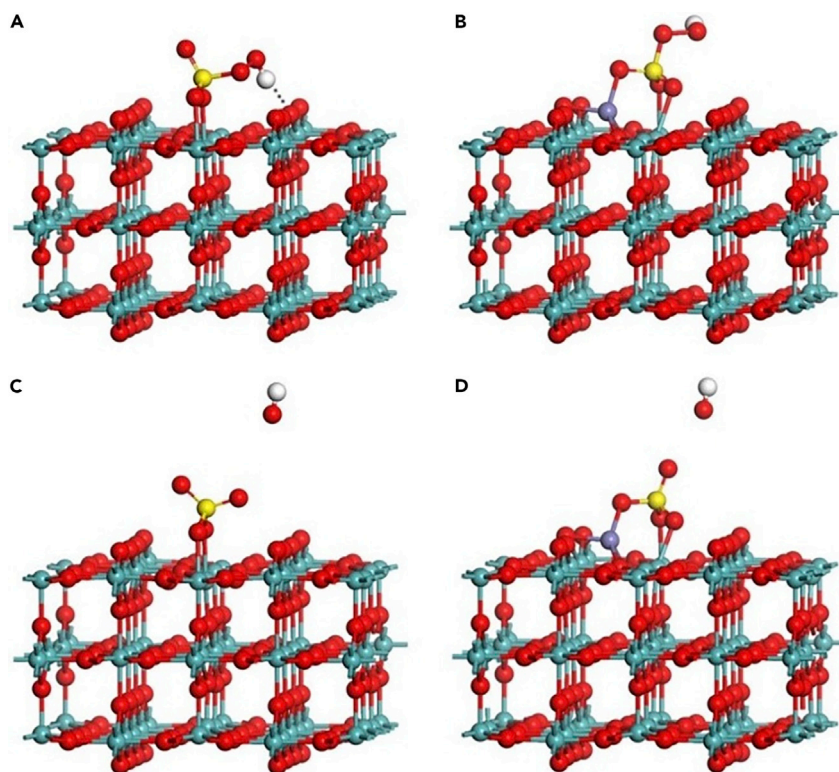
Figure 4. DFT Calculation of PMS Activation on MoO$_2$ (110) Surface

The optimal adsorption configuration of PMS and its decomposition on MoO$_2$ (110) surfaces, respectively. Only side views are presented here: (A) HSO$_5^-$ on the (110) surface, (B) HSO$_5^-$ on the Fe(II)-decorated (110) surface, (C) SO$_4^{2-}$+HO$^{\cdot}$ on the (110) surface, and (D) SO$_4^{2-}$ + HO$^{\cdot}$ on the Fe(II)-decorated (110) surface. The yellow, red, olive, purple, and white atoms are S, O, Mo, Fe, and H atoms, respectively.

Based on the above comprehensive characterization and DFT calculations (Figure 4), the mechanism of the L-RhB degradation can be inferred as follows: first, HSO$_5^-$ adsorbed on MoO$_2$ surface under acidic conditions, followed by Fe(II) approaching the surface owing to its positive charge. Subsequently, Fe(II) donates one electron to HSO$_5^-$ transforming into Fe(III). Therefore, HSO$_5^-$ is dissociated into the radical species ($^{\cdot}$OH and SO$_4^{\cdot-}$) to attack the organic molecules. These results are supported by the rapid decline of Fe(II) in the first minute (Figure 2D) and the EPR signals of DMPO$^{\cdot}$-OH and DMPO$^{\cdot}$-SO$_4^-$ adducts (Figure 2B). Afterward, the organic compounds are mineralized by those radical species, and Fe(III) is reduced to Fe(II) by Mo(IV) on the surface of the MoO$_2$ to continue activating PMS at the same time. Moreover, PMS is also decomposed to produce SO$_5^{\cdot-}$ as a by-product. This cocatalytic mechanism of MoO$_2$ in the PMS/Fe(II)/MoO$_2$ system is schematically summarized in Figure 5A.

High-performance liquid chromatography (HPLC) was employed to analyze the primary products after the L-RhB degradation in the PMS/Fe(II)/MoO$_2$ system. As shown in Figure 5B, the strongest peak at 14.02 min, which corresponds to complete disappearance of L-RhB molecules after the oxidation reaction, confirms its complete degradation. Moreover, the PMS/Fe(II)/MoO$_2$ system achieved relatively a high total organic carbon (TOC) removal rate (50%) with the addition of 0.650 mM PMS per 30 min, as illustrated in Figure 5C. This method may be an appropriate way for further mineralization of intermediates to H$_2$O and CO$_2$ (Zou et al., 2013).

Due to the complex structure of L-RhB, we explored the degradation intermediates and mechanisms of phenol, another organic pollutant that can be degraded in the PMS/Fe(II)/MoO$_2$ system. Based on the fragment peaks obtained from gas chromatography-mass spectrometry (GC-MS) measurements (Figure S6), we speculated that mainly SO$_4^{\cdot-}$ and $\cdot$OH would attack the benzene ring first to form phenoxy radicals, thereby producing a series of ring-opening reactions, as speculative in the oxidation reaction
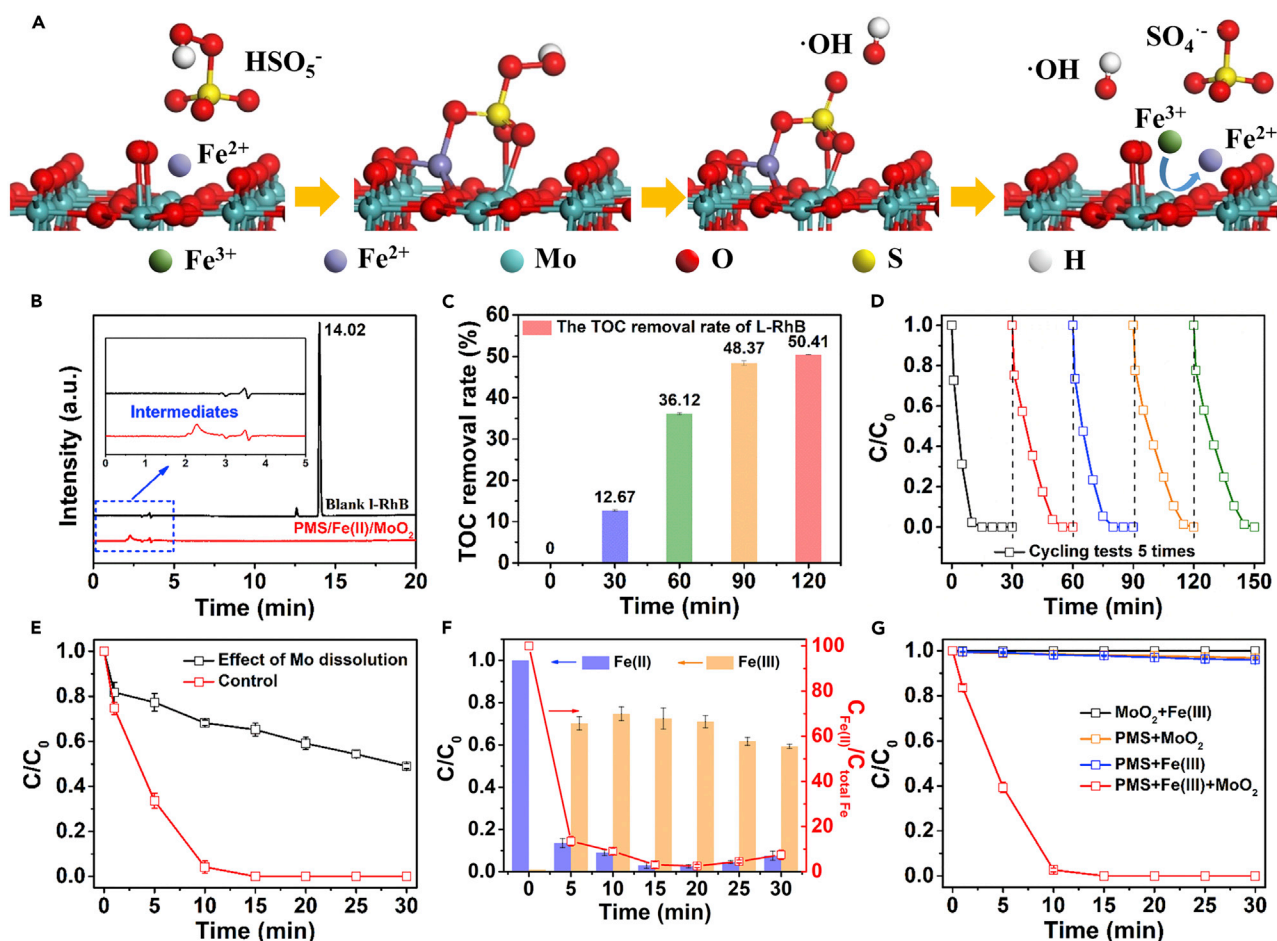
Figure 5. Mineralization Ability of PMS/Fe(II)/MoO$_2$ System and Cyclic Stability of MoO$_2$

(A) Mechanism of MoO$_2$ accelerating Fe(III)/Fe(II) cycle and promoting PMS activation; (B) HPLC signals of L-RhB and intermediates; (C) TOC removal rate with 0.650 mM PMS added per 30 min; (D) cycling test of MoO$_2$ (after UV irradiation); (E) effect of dissolved Mo ions on the degradation of L-RhB in PMS/Fe(II)/MoO$_2$ system; (F) the variation in Fe(II) and Fe(III) concentration in PMS/Fe(II)/dissolved Mo system; (G) degradation of different L-RhB concentration in PMS/Fe(III)/MoO$_2$ system. General conditions: [PMS]$_0$ = 0.650 mM, [Fe(II)]$_0$ = 0.036 mM (total Fe) or [Fe(III)]$_0$ = 0.035 mM, [MoO$_2$]$_0$ = 300 mg/L, initial pH = 3.0, [L-RhB]$_0$ = 20 mg/L. Error bars represent the standard deviation from at least duplicate experiments.

pathway depicted in Scheme S1. However, the fragment (m/z = 73) with the strongest molecular ion peak could be attributed to glyoxylic acid intermediate, which is known to resist mineralization (Pimentel et al., 2008).

The reusability of MoO$_2$ is a very important aspect for commercial pollutants treatment. The cocatalytic activity of MoO$_2$ was greatly reduced in the second cycle as shown in Figure 5D. Vacuum calcination was employed to restore the activity of MoO$_2$. As shown in Figure S7, the activity of MoO$_2$ after vacuum calcination was still much worse than the original. Therefore, we suspect that the active sites on the surface of MoO$_2$ were covered by carbon deposits, which were difficult to remove, but after UV irradiation of MoO$_2$, its cocatalytic activity was restored, which could be attributed to the decomposition of some unmineralized carbon-based residues on MoO$_2$ surface. Hence, its cocatalytic activity remained stable for the next three recycles.

Subsequently, the amount of the dissolved Mo ions under acidic conditions was determined. Figure S8 shows that the dissolution balance of Mo ions (1.60 mg/L, 0.71% of the total Mo addition) was achieved in 120 min. Because each experiment ended in 30 min, and the dissolved Mo ions might be the primary cocatalyst in reducing Fe(III) rather than MoO$_2$ itself, the degradation of L-RhB and the variation of Fe(II) and Fe(III) concentrations were measured in the PMS/Fe(II)/dissolved Mo ion system. As shown in Figure 5E,

the degradation rate of L-RhB dropped sharply, with only 51.9% degraded in 30 min, which is far slower than that in the PMS/Fe(II)/MoO$_2$ system. This demonstrates that the main cocatalytic effect in the PMS/Fe(II)/MoO$_2$ system comes from Mo(IV) on the surface of MoO$_2$ rather than the dissolved Mo ions. Also, the variations of Fe(II) and Fe(III) concentrations can explain the poor performance of the PMS/Fe(II)/dissolved Mo ion system. As shown in Figure 5F, almost no Fe(II) was recovered after 30 min, whereas Fe(III) concentration remained almost constant similar to the PMS/Fe(II) system, which could be correlated to the low conversion rate of Fe(III)/Fe(II), confirming that the few dissolved Mo ions were not sufficient to promote rapid Fe(III)/Fe(II) conversion.

Ultimately, a large scale-up test with 1 L system was employed to examine the practicality in scaling-up the PMS/Fe(II)/MoO$_2$ system for practical environmental remediations. As shown in Figure S9, PMS/Fe(II)/MoO$_2$ system maintained its excellent catalytic performance compared with the PMS/Fe(II) system even in this large volume, consistent with results in Figure 1A. Moreover, we found that 12 times the amount of Fe(II) (40 mg/L per 10 min added) was required to make the degradation effect of PMS/Fe(II) system almost same as that of PMS/Fe(II)/MoO$_2$ system. Therefore, the addition of MoO$_2$ reduced the amount of Fe(II) needed by more than 92% and subsequently reduced the generation of iron sludge and the cost of secondary pollution treatment. Taking one ton of this wastewater as an example, the consumption of PMS and Fe(II) in MS/Fe(II) system was 0.82 \$ and 0.17 \$, respectively. And the consumption of PMS and Fe(II) in PMS/Fe(II)/MoO$_2$ system was 0.82 \$ and 0.01 \$. Considering that the amount of PMS added to the two systems is the same, the cost difference between the two systems is mainly due to the amount of iron added. Therefore, the addition of cocatalyst can save 94% of the cost. This shows the great potentials of the PMS/Fe(II)/MoO$_2$ system for industrial applications.

Expanded Application of MoO$_2$ in PMS/Fe(III) System

In general, Fe(III) does not readily activate PMS according to Equation 2. However, because the addition of MoO$_2$ significantly promotes the conversion of Fe(III) to Fe(II), it should enhance the decomposition of PMS in PMS/Fe(III) system. To examine this hypothesis, we carried a series of testing for the degradation of L-RhB in PMS/Fe(III)/MoO$_2$ system as shown in Figure 5G. The obtained results were far better than the PMS/Fe(III) system (4.1%) and the PMS/MoO$_2$ system (3.3%), where no degradation was observed in the Fe(III)/MoO$_2$ system. This might be because Fe(III) was reduced to Fe(II) immediately after the addition of MoO$_2$, leading to its spontaneously precipitation. Therefore, the performance of the degradation of L-RhB is substantially the same as that in the PMS/MoO$_2$/Fe(II) system. Figures S10 and S11 show the great degradation performance of L-RhB and other organics, and Figure S12 shows the almost same kinetic results as PMS/MoO$_2$/Fe(II) system. The degradation of L-RhB in different pH was also investigated as shown in Figure S13. Radical quenching tests proved that SO$_4^{\cdot-}$ was the main reactive species (Figure S14), which was further supported by EPR spectra (Figure S16). Typically, as shown in Figure S15, as the reaction progressed, Fe(III) rapidly decreased and Fe(II) gradually increased, but the total amount of iron ions detected after starting the reaction was lower than initially added. This may be because in the presence of PMS and MoO$_2$, Fe(II) was rapidly oxidized by PMS, and Fe(III) was also rapidly reduced by MoO$_2$, so that 1,10-phenanthroline and KSCN were difficult to capture Fe(II) or Fe(III) quickly. The result proves the circulation of iron ions during the reaction in PMS/Fe(III)/MoO$_2$ system. The oxidation mechanism of L-RhB in the PMS/Fe(III)/MoO$_2$ system is also basically the same as that of PMS/Fe(II)/MoO$_2$ system, which was supported by SEM images (Figure S17), XRD patterns (Figure S18), Raman spectra (Figure S19), and XPS spectra (Figures S20–S22). The only difference that might exist is that in the PMS/Fe(III)/MoO$_2$ system, MoO$_2$ reduces the surface-adsorbed Fe(III) to Fe(II) first and then activates PMS.

DISCUSSION

The slow transformation from Fe(III) to Fe(II) has persistently limited the practical application of PMS/Fe(II) systems, for which a great amount of iron ions are needed to activate PMS, causing massive formation of iron sludge. In the PMS/Fe(II)/MoO$_2$ system, this problem is solved by the addition of MoO$_2$, which is earth-abundant, quite stable, and has enough reductive power to reduce Fe(III). Therefore, an extremely low concentration of Fe(II) (0.036 mM) is adequate to activate PMS and degrade organic pollutants rapidly in the wide pH range of 2.0–9.0. The iron sludge is limited so that no more secondary pollution is caused. SO$_4^{\cdot-}$ and $^{\cdot}$OH are the primary reactive species produced in the PMS/Fe(II)/MoO$_2$ system. The TOC removal rate of L-RhB reached 50% with the addition of PMS, which will be an appropriate approach to completely mineralize refractory organic contaminants. Moreover, MoO$_2$ could be recycled and exhibited excellent

recover activity after its treatment with UV light irradiation. The involvement of MoO_2 in the PMS/Fe(II) system could allow for the low-cost remediation of organic pollutants, thus contributing to sustainable development for the environment.

Limitations of the Study

Although this study greatly accelerates the activation of PMS and reduces secondary pollution compared with some other systems, the amount of catalyst needed for the reaction is relatively high. Fe(II) is inevitably needed to activate PMS because MoO_2 itself cannot activate PMS.

METHODS

All methods can be found in the accompanying Transparent Methods supplemental file.

SUPPLEMENTAL INFORMATION

Supplemental Information can be found online at https://doi.org/10.1016/j.isci.2020.100861.

AUTHOR CONTRIBUTIONS

M.X. conceived and designed the research. J.J. conducted all the experiments. H.D. carried out the theoretical calculations. J.J. and M.X. wrote the paper. Y.Y., R.A., and J.Z. gave suggestions on the experiment and writing. All authors discussed and analyzed the data.

DECLARATION OF INTERESTS

The authors declare no competing financial interest.

REFERENCES

Al-Ghouti, M.A., Khraisheh, M.A.M., Allen, S.J., and Ahmad, M.N. (2003). The removal of dyes from textile wastewater: a study of the physical characteristics and adsorption mechanisms of diatomaceous earth. J. Environ. Manage. 69, 229–238.

Anipsitakis, G.P., and Dionysiou, D.D. (2003). Degradation of organic contaminants in water with sulfate radicals generated by the conjunction of peroxymonosulfate with cobalt. Environ. Sci. Technol. 37, 4790–4797.

Anipsitakis, G.P., and Dionysiou, D.D. (2004). Radical generation by the interaction of transition metals with common oxidants. Environ. Sci. Technol. 38, 3705–3712.

Barros, D., Bouchet, J., Raoult, I., Mogne, T., Martin, J.M., Kasrai, M., and Yamada, Y. (2003). Friction reduction by metal sulfides in boundary lubrication studied by XPS and XANES analyses. Wear 254, 863–870.

Brandt, B.G. (1971). On the Crystal Structures of MoO_2 and $MoO_3.2H_2O$: An Account of Computer Programming and Structure Refinement (University).

Buck, C., Skillen, N., Robertson, J., and Robertson, P.K.J. (2018). Photocatalytic OH radical formation and quantification over TiO_2 P25: producing a robust and optimised screening method. Chin. Chem. Lett. 29, 773–777.

Camacho-López, M.A., Escobar-Alarcón, L., Picquart, M., Arroyo, R., Córdoba, G., and Haro-Poniatowski, E. (2011). Micro-Raman study of the m-MoO_2 to α-MoO_3 transformation induced by cw-laser irradiation. Opt. Mater. 33, 480–484.

Chen, C., Zuo, W., Yang, J., Cui, H., and Fu, M. (2016). Yolk–shell structured $CoFe_2O_4$ microspheres as novel catalysts for peroxymonosulfate activation for efficient degradation of butyl paraben. RSC Adv. 6, 101361–101364.

Chen, J., Fang, C., Xia, W., Huang, T., and Huang, C. (2018). Selective transformation of $\hat{l}^2$-Lactam antibiotics by peroxymonosulfate: reaction kinetics and non-radical mechanism. Environ. Sci. Technol. 52, 1461–1470.

Clarizia, L., Russo, D., Somma, I.D., Marotta, R., and Andreozzi, R. (2017). Homogeneous photo-Fenton processes at near neutral pH: a review. Appl. Catal. B Environ. 209, 358–371.

Crini, G. (2006). Non-conventional low-cost adsorbents for dye removal: a review. Bioresour.Technol. 97, 1061–1085.

Dai, D., Yang, Z., Yao, Y., Chen, L., Jia, G., and Luo, L. (2017). Highly efficient removal of organic

contaminant based on peroxymonosulfate activation by iron phthalocyanine: mechanism and bicarbonate ion enhancement effect. Catal. Sci. Technol. *7*, 934–942.

Dan, C., Ma, X., Zhou, J., Xi, C., and Qian, G. (2014). Sulfate radical-induced degradation of Acid Orange 7 by a new magnetic composite catalyzed peroxymonosulfate oxidation process. J. Hazard. Mater. *279*, 476–484.

Dong, C., Liu, J., Xing, M., and Zhang, J. (2018). Development of titanium oxide-based mesoporous materials in photocatalysis. Res. Chem. Intermediat. *44*, 7079–7091.

Du, J., Bao, J., Liu, Y., Kim, S.H., and Dionysiou, D.D. (2018a). Facile preparation of porous Mn/Fe_3O_4 cubes as peroxymonosulfate activating catalyst for effective bisphenolA degradation. Chem. Eng. J. https://doi.org/10.1016/j.cej.2018.05.177.

Du, M., Qiu, B., Zhu, Q., Xing, M., and Zhang, J. (2018b). Cobalt phosphide nanocages encapsulated with graphene as ultralong cycle life anodes for reversible lithium storage. Res. Chem. Intermediat. *44*, 7847–7859.

Duan, X., Su, C., Miao, J., Zhong, Y., Shao, Z., Wang, S., and Sun, H. (2018). Insights into perovskite-catalyzed peroxymonosulfate activation: maneuverable cobalt sites for promoted evolution of sulfate radicals. Appl. Catal. B Environ. *220*, 626–634.

Fang, G., Liu, C., Wang, Y., Dionysiou, D.D., and Zhou, D. (2017). Photogeneration of reactive oxygen species from biochar suspension for diethyl phthalate degradation. Appl. Catal. B Environ. *214*, 34–45.

Furman, O.S., Teel, A.L., and Watts, R.J. (2010). Mechanism of base activation of persulfate. Environ. Sci. Technol. *44*, 6423–6428.

Ghanbari, F., and Moradi, M. (2017). Application of peroxymonosulfate and its activation methods for degradation of environmental organic pollutants: Review. Chem. Eng. J. *310*, 41–62.

Guan, Y., Ma, J., Li, X., Fang, J., and Chen, L. (2011). Influence of pH on the formation of sulfate and hydroxyl radicals in the UV/peroxymonosulfate system. Environ. Sci. Technol. *45*, 9308–9314.

Hanawa, T., Hiromoto, S., and Asami, K. (2001). Characterization of the surface oxide film of a Co–Cr–Mo alloy after being located in quasi-biological environments using XPS. Appl. Surf. Sci. *183*, 68–75.

Harvey, A.E., Smart, J.A., and Amis, E.S. (1955). Simultaneous spectrophotometric determination of iron(II) and total iron with 1,10-phenanthroline. Anal. Chem. *27*, 26–29.

Hayon, E., Treinin, A., and Wilf, J. (1972). Electronic spectra, photochemistry, and autoxidation mechanism of the sulfite-bisulfite-pyrosulfite systems.SO_2^-, SO_3^-, SO_4^-, and SO_5^- radicals. J. Am. Chem. Soc. *94*, 47–57.

Herrera, L., Ruiz, P., Aguillon, J.C., and Fehrmann, A. (1989). A new spectrophotometric method for the determination of ferrous iron in the presence of ferric iron. J. Chem. Tech. Biotechnol. *44*, 171–181.

Hu, B., Mai, L., Wen, C., and Fan, Y. (2009). From MoO_3nanobelts to MoO_2nanorods: structure transformation and electrical transport. ACS Nano *3*, 478–482.

Hu, P., Su, H., Chen, Z., Yu, C., Li, Q., Zhou, B., Alvarez, P.J.J., and Long, M. (2017). Selective degradation of organic pollutants using an efficient metal-free catalyst derived from carbonized polypyrrole via peroxymonosulfate activation. Environ. Sci. Technol. *51*, 11288–11296.

Huang, G., Wang, C., Yang, C., Guo, P., and Yu, H. (2017). Degradation of bisphenol A by peroxymonosulfatecatalytically activated with $Mn_{1.8}Fe_{1.2}O_4$nanospheres: synergism between Mn and Fe. Environ. Sci. Technol. *51*, 12611–12618.

Ito, T., Adachi, Y., Yamanashi, Y., and Shimada, Y. (2016). Long-term natural remediation process in textile dye-polluted river sediment driven by bacterial community changes. Water Res. *100*, 458–465.

Khan, S., He, X., Khan, H.M., Boccelli, D., and Dionysiou, D.D. (2016). Efficient degradation of lindane in aqueous solution by iron (II) and/or UV activated peroxymonosulfate. J. Photochem. Photobiol. A *316*, 37–43.

Kusic, H., Peternel, I., Ukic, S., Koprivanac, N., Bolanca, T., Papic, S., and Bozic, A.L. (2011). Modeling of iron activated persulfate oxidation treating reactive azo dye in water matrix. Chem. Eng. J. *172*, 109–121.

Li, H., Shan, C., and Pan, B. (2018). Fe(III)-Doped g-C_3N_4 mediated peroxymonosulfate activation for selective degradation of phenolic compounds via high-valent iron-oxo species. Environ. Sci. Technol. *52*, 2197–2205.

Liang, C., and Su, H. (2009). Identification of sulfate and hydroxyl radicals in thermally activated persulfate. Ind. Eng. Chem. Res. *48*, 5558–5562.

Ling, S., Wang, S., and Peng, Y. (2010). Oxidative degradation of dyes in water using Co^{2+}/H_2O_2 and Co^{2+}/peroxymonosulfate. J. Hazard. Mater. *178*, 385–389.

Liu, J., Zhou, J., Ding, Z., Zhao, Z., Xu, X., and Fang, Z. (2017). Ultrasound irritation enhanced heterogeneous activation of peroxymonosulfate with Fe_3O_4 for degradation of azo dye. Ultrason. Sonochem. *34*, 953–959.

Muthuraman, G., and Teng, T.T. (2009). Extraction of methyl red from industrial wastewater using xylene as an extractant. Prog. Nat. Sci. *19*, 1215–1220.

Pignatello, J.J., Oliveros, E., and MacKay, A. (2006). Advanced oxidation processes for organic contaminant destruction based on the fenton reaction and related chemistry. Crit. Rev. Environ. Sci. Technol. *36*, 1–84.

Pimentel, M., Oturan, N., Dezotti, M., and Oturan, M.A. (2008). Phenol degradation by advanced electrochemical oxidation process electro-Fenton using a carbon felt cathode. Appl. Catal. B Environ. *83*, 140–149.

Rastogi, A., Al-Abed, S.R., and Dionysiou, D.D. (2009a). Effect of inorganic, synthetic and

naturally occurring chelating agents on Fe(II) mediated advanced oxidation of chlorophenols. Water Res. *43*, 684–694.

Rastogi, A., Al-Abed, S.R., and Dionysiou, D.D. (2009b). Sulfate radical-based ferrous–peroxymonosulfate oxidative system for PCBs degradation in aqueous and sediment systems. Appl. Catal. B Environ. *85*, 171–179.

Sheng, B., Yang, F., Wang, Y., Wang, Z., Li, Q., Guo, Y., Lou, X., and Liu, J. (2019). Pivotal roles of MoS_2 in boosting catalytic degradation of aqueous organic pollutants by Fe(II)/PMS. Chem. Eng. J. *375*, 121989.

Sun, Y., Hu, X., Luo, W., and Huang, Y. (2011). Self-assembled hierarchical MoO_2/graphenenanoarchitectures and their application as a high-performance anode material for lithium-ion batteries. ACS Nano *5*, 7100–7107.

Tang, R., Jiang, C., Qian, W., Jian, J., Zhang, X., Wang, H., and Yang, H. (2015). Dielectric relaxation, resonance and scaling behaviors in $Sr_3Co_2Fe_{24}O_{41}$hexaferrite. Sci. Rep. *5*, 13645–13655.

Tao, X., Ma, W., Zhang, T., and Zhao, J. (2001). Efficient photooxidative degradation of organic compounds in the presence of iron tetrasulfophthalocyanine under visible light irradiation. Angew.Chem. Int. Ed. *40*, 3014–3016.

Timmins, G.S., Liu, K.J., Bechara, E.J., Kotake, Y., and Swartz, H.M. (1999). Trapping of free radicals with direct in vivo EPR detection: a comparison of 5, 5-dimethyl-1-pyrroline-N-oxide and 5-diethoxyphosphoryl-5-methyl-1-pyrroline-N-oxide as spin traps for HO and $SO_4^{\cdot-}$. Free Radic. Biol. Med. *27*, 329–333.

Tokarz-Sobieraj, R., Gryboś, R., and Witko, M. (2011). Electronic structure of MoO_2. DFT periodic and cluster model studies. Appl. Catal. A.Gen. *391*, 137–143.

Ugo, P., Moretto, L.M., De Boni, A., Scopece, P., and Mazzocchin, G.A. (2002). Iron (II) and iron (III) determination by potentiometry and ion-exchange voltammetry at ionomer-coated electrodes. Anal. Chim. Acta *474*, 147–160.

Wacławek, S., Grübel, K., and Černík, M. (2015). Simple spectrophotometric determination of monopersulfate. Spectrochim. Acta A *149*, 928–933.

Wang, S., Xu, W., Wu, J., Gong, Q., and Xie, P. (2020). Improved sulfamethoxazole degradation by the addition of MoS_2 into the Fe^{2+}/peroxymonosulfate process. Sep. Purif. Technol. *235*, 116170.

Xia, X., Deng, S., Xie, D., Wang, Y., Feng, S., Wu, J., and Tu, J. (2018). Boosting sodium ion storage by anchoring MoO_2 on vertical graphene arrays. J. Mat. Chem. A *6*, 15546–15552.

Xie, X., Lin, L., Liu, R.Y., Jiang, Y.F., Zhu, Q., and Xu, A.W. (2015). The synergistic effect of metallic molybdenum dioxide nanoparticle decorated graphene as an active electrocatalyst for an enhanced hydrogen evolution reaction. J. Mater. Chem. A *3*, 8055–8061.

Xing, M., Xu, W., Dong, C., Bai, Y., Zeng, J., Zhou, Y., Zhang, J., and Yin, Y. (2018). Metal sulfides as

excellent cocatalysts for H_2O_2 decomposition in advanced oxidation processes. Chem 4, 1359–1372.

Yang, X., Cheng, X., Elzatahry, A.A., Chen, J., Alghamdi, A., and Deng, Y. (2019). Recyclable Fenton-like catalyst based on zeolite Y supported ultrafine, highly-dispersed Fe_2O_3 nanoparticles for removal of organics under mild conditions. Chin. Chem. Lett. 30, 324–330.

Yi, Q., Ji, J., Shen, B., Dong, C., Liu, J., Zhang, J., and Xing, M. (2019). Singlet oxygen triggered by superoxide radicals in a molybdenum cocatalytic fenton reaction with enhanced REDOX activity in the environment. Environ. Sci. Technol. 53, 9725–9733.

Yi, Q., Zhou, Y., Xing, M., and Zhang, J. (2015). Vacuum activation-induced Ti^{3+} and carbon codoped TiO_2 with enhanced solar light photo-catalytic activity. Res. Chem. Intermediat. 42, 4181–4189.

Yun, E.T., Lee, J.H., Kim, J., Park, H.D., and Lee, J. (2018). Identifying the nonradical mechanism in the peroxymonosulfate activation process: singlet oxygenation versus mediated electron transfer. Environ. Sci. Technol. 52, 7032–7042.

Zamora, P.L., and Villamena, F.A. (2012). Theoretical and experimental studies of the spin trapping of inorganic radicals by 5,5-dimethyl-1-pyrroline N-oxide (DMPO). 3. Sulfur dioxide, sulfite, and sulfate radical anions. J. Phys. Chem. A 116, 7210–7218.

Zhang, T., Chen, Y., and Leiknes, T. (2016). Oxidation of refractory benzothiazoles with PMS/$CuFe_2O_4$: kinetics and transformation intermediates. Environ. Sci. Technol. 50, 5864–5873.

Zhang, M., Chen, M., Bi, Y., Huang, L., Zhou, K., and Zheng, Z. (2019). A bimetallic Co_4Mo_8 cluster built from Mo_8oxothiomolybdate capped by a Co_4-thiacalix[4]arene unit: the observation of the Co–Mo synergistic effect for binder-free electrocatalysts. J. Mat. Chem. A 7, 12893–12899.

Zou, J., Ma, J., Chen, L., Li, X., Guan, Y., Xie, P., and Pan, C. (2013). Rapid acceleration of ferrous iron/peroxymonosulfate oxidation of organic pollutants by promoting Fe(III)/Fe(II) cycle with hydroxylamine. Environ. Sci. Technol. 47, 11685–11691.

Supplemental Information

Metallic Active Sites on MoO$_2$(110) Surface

to Catalyze Advanced Oxidation Processes

for Efficient Pollutant Removal

Jiahui Ji, Rashed M. Aleisa, Huan Duan, Jinlong Zhang, Yadong Yin, and Mingyang Xing

1 **Supplemental Information**

2

3

4 **Metallic Active Sites on MoO$_2$ (110) Surface to Catalyze**

5 **Advanced Oxidation Processes for Efficient Pollutant**

6 **Removal**

7 **Jiahui Ji, Rashed M. Aleisa, Huan Duan, Jinlong Zhang, Yadong Yin and**
8 **Mingyang Xing**

9

10

11

12

13

14

15

16

17

18

19

20

21

22

23

SUPPLEMENTAL

25 **Transparent Methods**

26 **Materials.** All chemicals, including molybdenum dioxide (MoO_2, Shanghai Energy

27 Chemical Co., Ltd., 99%), ferrous sulfate heptahydrate ($FeSO_4 \cdot 7H_2O$, Shanghai

28 Aladdin Bio-Chem Technology Co., Ltd., 99.95%), potassium monopersulfate triple

29 salt ($KHSO_5 \cdot 0.5KHSO_4 \cdot 0.5K_2SO_4$, PMS, Shanghai Macklin Biochemical Co., Ltd., 42%

30 ~ 46% $KHSO_5$ basis), Lissamine rhodamine B (L-RhB, Shanghai Aladdin Bio-Chem

31 Technology Co., Ltd.), phenol (Shanghai Aladdin Bio-Chem Technology Co., Ltd., $\geq$

32 99%), methylene blue (MB, Shanghai Adamas Reagent Co., Ltd., RG, $\geq$ 98%),

33 sulfadiazine (Shanghai Aladdin Bio-Chem Technology Co., Ltd., 98%), norfloxacin

34 (Shanghai Aladdin Bio-Chem Technology Co., Ltd., 98%) 1,10-phenanthroline

35 (Shanghai Lingfeng Chemical Reagent Co., Ltd., $\geq$ 99%), sodium hydroxide (NaOH,

36 Shanghai Titan Scientific Co. Ltd., AR, $\geq$ 96.0%), sulfuric acid (H_2SO_4, Shanghai Titan

37 Scientific Co. Ltd., CP, 95.0% ~ 98.0%), methanol (MeOH, Shanghai Aladdin Bio-

38 Chem Technology Co., Ltd., AR, 99.5%), tert-butyl alcohol (TBA, Shanghai Aladdin

39 Bio-Chem Technology Co., Ltd., GR, $\geq$ 99.5%), benzoic acid (Shanghai Lingfeng

40 Chemical Reagent Co., Ltd., AR, $\geq$ 99.5%), 5,5-dimethyl-1-pyrroline N-oxide (DMPO,

41 Shanghai Adamas Reagent Co., Ltd., RG, $\geq$ 98%) and potassium thiocyanate (KSCN,

42 Shanghai Titan Scientific Co. Ltd., AR, $\geq$ 98.5%), were used without further

43 purification. Deionized water (DI-water) was produced by OKP-S040 Standard

44 ultrapure water system and used in all experiments.

45 **Experimental Procedures.** All experiments were performed in plastic cups with

46 magnetic stirring to keep the solution homogeneous during the reaction. The

47 predesigned initial pH of the L-RhB solution was adjusted first with NaOH,

48 H_2SO_4 or buffer solutions. Then, fixed amounts of MoO_2 and $FeSO_4 \cdot 7H_2O$ were

49 added to 100 mL reaction solutions with the desired concentration of organic

50 pollutants. Finally, quantitative PMS was added to initiate the oxidation. Samples

51 were taken out at regular intervals, centrifuged and analyzed immediately. The

52 stability of MoO_2 was also investigated. After being centrifuged, washed, dried

53 and vacuum calcination/UV (365 nm)-activated, MoO_2 continued to participate

54 in the next degradation reaction.

55 Radical quenching tests. Radical quenching tests were conducted to identify the

56 dominant radicals in PMS/Fe(II)/MoO_2 system with methanol and TBA, which

57 were added before the addition of PMS. The other procedures were the same as

58 the experiments above. The radical species were further detected by electron

59 paramagnetic resonance (EPR) technology, where 5,5-dimethyl-1-pyrroline

60 (DMPO) was used as a spin-trapping reagent. The detailed parameters were as

61 follows: a center field of 352.0 mT, a sweep width of 20.0 mT, a microwave

62 frequency of 9.882 GHz, a microwave power of 6.402 mW, a temperature of

63 300.0 K, a receiver gain of 7.96×10^4, a modulation amplitude of 0.1 mT, and a

64 sweep time of 41.94 s.

65 The variety of iron ions concentrations. The variety of Fe(II) or Fe(III)

66 concentration was tracked during the reaction by complexing the samples with 1,

67 10-phenanthroline or potassium thiocyanate (KSCN), respectively. Fe(II) and

68 Fe(III) can be complexed with 1,10-philoxene and KSCN for color development,

69 respectively. Since the concentration of the complex is proportional to the

70 absorbance, the corresponding absorbance of Fe(II)/Fe(III)-complex with the

71 initial known concentration was measured. Thus, the content of Fe(II)/Fe(III) can

72 be calculated from the ratio of the absorbance of the complex to the absorbance

73 of the initial complex at different time periods: The L-RhB solution was replaced

74 by deionized water while the other conditions and procedures remained

75 unchanged; excessive 1,10-phenanthroline or potassium thiocyanate reagent was

76 immediately added after sampling and centrifuging, and then analyzed.

77 The effect of dissolved Mo ions. Moreover, in order to investigate the effect of

78 dissolved Mo ions for (i) the conversion of Fe(III)/Fe(II) and (ii) the degradation

79 of L-RhB, the following experiments were also explored: MoO_2 was added first

80 in (i) deionized water or (ii) L-RhB solution at fixed initial pH. Then, the solution

81 was stirred for 30 min to dissolute Mo ions and centrifuged to remove solid MoO_2.

82 Finally, $FeSO_4 \cdot 7H_2O$ and PMS was added to initiate the reaction. (i) Excessive

83 1,10-phenanthroline reagent was immediately added after sampling and

84 centrifuging, and then analyzed; (ii) samples were taken out at regular intervals,

85 centrifuged and analyzed immediately.

86 All the experiments in PMS/Fe(III)/MoO$_2$ system were the same as those in

87 PMS/Fe(II)/MoO$_2$ system, just using Fe(III) to replace Fe(II).

88 **Analytic Methods.** The concentrations of L-RhB, MB, Fe(II) and Fe(III) were

89 measured with a UV-Vis spectrophotometer (SHIMADZU UV-2450). The pH

90 value and pH variation of the solution during the reaction were determined with

91 a pH meter (INESA PHS-3C). The zeta potential of MoO$_2$ was measured for its

92 isoelectric point (IEP) by a ZETASIZER instrument (Malvern ZEN3600). The

93 morphology of MoO$_2$ was characterized by scanning electron microscope (SEM,

94 JEOL JSM-6360 LV). X-ray diffraction (XRD) patterns were acquired in the

95 range of 5-80° (2θ) by a RigakuD/MAX 2550 diffractometer, with the operation

96 parameters of 40 kV and 100 mA and Cu Kα radiation (λ = 1.5406 Å). Raman

97 spectroscopy was done using a Renishaw Invia spectrometer using a 532 nm Ar$^+$

98 laser at room temperature. X-ray photoelectron spectroscopy (XPS) of MoO$_2$ was

99 conducted at a condition of Al Kα irradiation by THERMO ESCALAB 250 Xi.

100 The total organic carbon (TOC) concentration of the filterable degradation agent

101 was investigated using the SHIMADZU TOC-L CPN analyzer. The dissolved

102 Mo ions in acidic conditions were detected by an inductively coupled plasma

103 atomic emission spectrometer (ICP, NYSE: A 725). A PC fluorescence

104 spectrophotometer (SHIMADZU RF-5301) was employed to obtain the

105 photoluminescence (PL) spectroscopy of hydroxybenzoic acid to detect $^•$OH. A

106 high-performance liquid chromatography (HPLC, SHIMADZU LC-20A) were

107 employed to explore the degradation of L-RhB, phenol, sulfadiazine and

norfloxacin. A gas chromatography-mass spectrometer (GC-MS, ThermoFisher

Trace ISQLT) with HP-5ms column (30 m * 250 um * 0.25 um) was employed

to explore the intermediates in the degradation process of phenol. The heating

program was maintained at 40 ℃ for 3 min, heated to 300 ℃ at 5 ℃/min, and

held for 10 min. The inlet temperature was 300 ℃, the transfer line temperature

was 300 ℃, and the column flow rate was 1.2 mL/min. Mass spectrometry

conditions: EI ionization source (70 eV, full scan).

DFT calculation. Computational details. Density functional theory (DFT) calculations

were carried out using the all-electron code Fritz-Haber Institute ab initio molecules

simulations package (FHI-aims).(Blum et al., 2009) Interactions between atomic core

shells and the valence electrons were described using the projector-augmented wave

(PAW) method, the Perdew-Burke-Ernzerh (PBE) of gradient-corrected functional was

used to treat the exchange and correlation. (Perdew, 1996, Kresse, 1999) The default

"tight" species were chosen in this work. Considering the weak non-covalent van der

Waals attraction, all calculations were performed by the scheme of Tkatchenko and

Scheffler. (Tkatchenko and Scheffler, 2009) Gaussian smearing was used with a width

of 0.1 eV to determine the partial occupancies. The convergence threshold was set to

be 10^{-5} eV in energy and 10^{-3} eV·Å^{-1} in force. A periodic (110) slab model of MoO_2

was built up to simulate the activation process of peroxymonosulfate (PMS) molecules,

which preferred to adsorb on the (110) surfaces, contributed to the electron transfer and

the generation of hydroxyl radicals. Besides, the catalytic effect of Fe(II) ions was also

taken into account for low surface coverages of PMS molecules. To minimize the

130   interaction of (110) surfaces in different supercells along c direction, a 20 Å vacuum

131   layer between them was taken. All atoms were allowed to relax expected the bottom

132   three-layer atoms to fix at the bulk parameters. Brillouin zone was sampled using a

133    $3 \times 3 \times 1$ Monkhorst Pack k-point mesh during geometry optimization and properties

134   calculation for the (110) surface of MoO_2. (Monkhorst, 1976)

135   Adsorption energy and charge transfer. To reveal the activation process of PMS

136   molecule on the (110) surface of MoO_2, the interaction between them could be

137   evaluated by the adsorption energies, which was defined as $\Delta E_{ads}=E_{MoO_2+PMS}-$

138    $E_{MoO_2}-E_{PMS}$, where E_{MoO_2+PMS} was the total energy for the PMS adsorbed on

139   the surface, E_{MoO_2} was the total energy for the MoO_2 substrate without

140   adsorption, and E_{PMS} was the total energy of a separated molecule as

141   determined from DFT calculations. The Mulliken charge analysis was used to

142   quantitatively estimate the amount of charge transfer between the adsorbed

143   molecule and MoO_2 substrate, which contributed to reveal the activation

144   mechanism. (Tang et al., 2009)

145

146

147

148

149
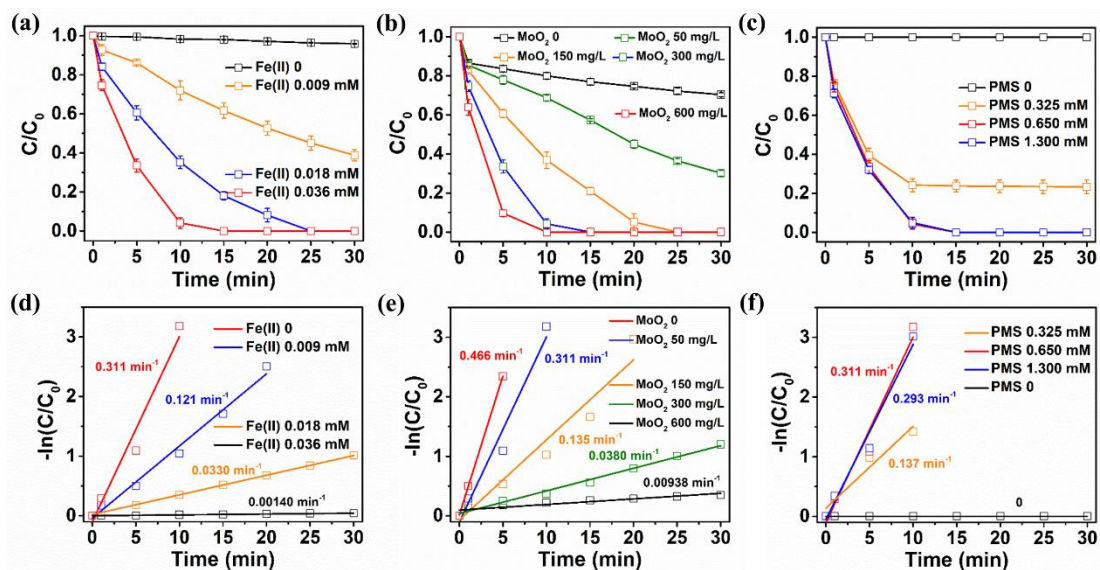
Figure S1. Effect of (a) Fe(II) concentration, (b) MoO_2 concentration, (c) PMS concentration on L-RhB oxidation in PMS/Fe(II)/MoO_2 system; Pseudo-first-order kinetics of effect of (d) Fe(II), (e) MoO_2 and (f) PMS concentration. General conditions: $[PMS]_0 = 0.650$ mM, $[Fe(II)]_0 = 0.036$ mM, $[MoO_2]_0 = 300$ mg/L, initial pH = 3.0, [L-RhB]_0 = 20 mg/L. Error bars represent the standard deviation from at least duplicate experiments. Related to Figure **1**.
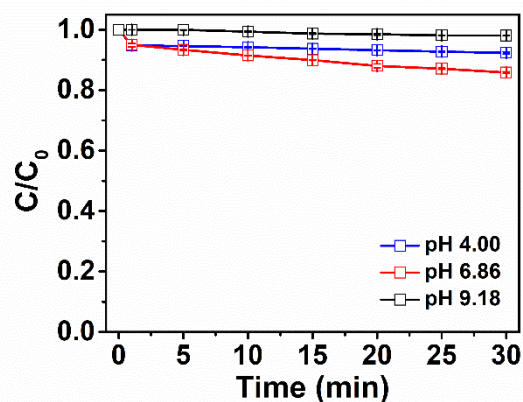
Figure S2. The investigation of the influence of solution pH with potassium hydrogen phthalate ($C_8H_5KO_4$, pH 4.00), mixed phosphate (pH 6.86) and borax ($Na_2B_4O_7 \cdot 10H_2O$, pH 9.18) buffer solutions, respectively. General conditions: $[PMS]_0 = 0.650$ mM, $[Fe(II)]_0 = 0.036$ mM, $[MoO_2]_0 = 300$ mg/L, initial pH = 3.0, $[L\text{-}RhB]_0 = 20$ mg/L. Error bars represent the standard deviation from at least duplicate experiments. Related to Figure **1**.
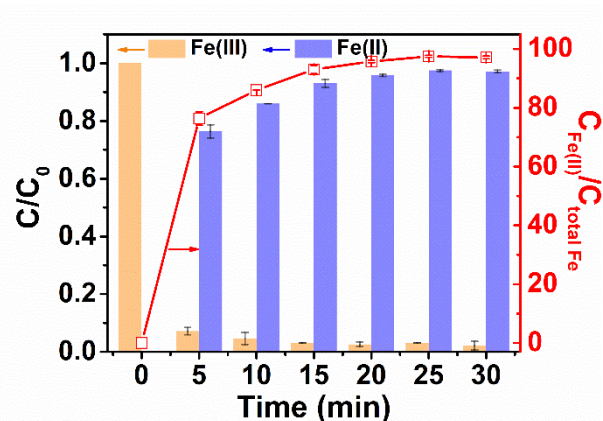
Figure S3. The variation of Fe(II) and Fe(III) concentrations in Fe(III)/MoO$_2$ system. General conditions: [Fe(III)]$_0$ = 0.035 mM (total Fe), [MoO$_2$]$_0$ = 300 mg/L, initial pH = 3.0. Error bars represent the standard deviation from at least duplicate experiments. Related to Figure **2**.

The reduction potential of Fe(III)/Fe(II) (0.77 V) is higher than that of MoO$_4^{2-}$/MoO$_2$ (0.65 V). As shown in Fig. S5, when MoO$_2$ was added to the Fe(III)-containing solution, Fe(III) was immediately reduced to Fe(II), which was almost completely reduced within 15 min. Thus, it can be concluded that MoO$_2$ itself can reduce Fe(III) to Fe(II), which solves the problem that iron ions are difficult to circulate in PMS/Fe(II) system.

Catalyst	Catalyst dosage	PMS concen.	Organic pollutant	Removal efficiency	Ref.
MoO$_2$/Fe(II) (this work)	0.30 g·L^{-1} /0.036 mM	0.65 mM	L-RhB; 20 mg·L^{-1}	96% in 10 min	-
HA/Fe(II)	0.4 mM /10.8 μM	0.32 mM	BA; 40 μM	94% in 15 min	(Zou et al., 2013)
Fe$_3$O$_4$@C/Co	0.20 g·L^{-1}	0.1 g·L^{-1}	AO II; 20 mg·L^{-1}	40 min	(Xu et al., 2015)
Fe$_3$O$_4$@MnO$_2$ BBHs	0.30 g·L^{-1}	20 mM	MB; 20 mg·L^{-1}	30 min	(Zhang et al., 2016)
Co$_3$[Fe(CN)$_6$]$_2$	50 mg·L^{-1}	50 mg·L^{-1}	RhB; 10 mg·L^{-1}	20 min	(Lin et al., 2016)
CNF3	0.10 g·L^{-1}	1.0 mM	4-CP; 0.10 mM	20 min	(Li et al., 2018a)
FeCo-LDH	0.20 g·L^{-1}	0.15 g·L^{-1}	RhB; 20 mg·L^{-1}	10 min	(Gong et al., 2017)
Fe$_3$O$_4$/Mn$_3$O$_4$/rGO	0.10 g·L^{-1}	0.30 g·L^{-1}	MB; 50 mg·L^{-1}	93.5% in 30 min	(Yang et al., 2015)
M@N-C (M=Fe, Co)	20 mg·L^{-1}	0.65 mM	Orange II; 20 mg·L^{-1}	90 min	(Yao et al., 2016)
CoFe$_2$O$_4$	0.40 g·L^{-1}	0.8 mM	ATZ; 10 mg·L^{-1}	30 min	(Li et al., 2018b)
Fe$_3$O$_4$@C/MnCo$_2$O$_4$	0.15 g·L^{-1}	0.06 g·L^{-1}	AO II; 20 mg·L^{-1}	99% in 15 min	(Lu et al., 2017)

217 **Table S1.** The catalytic performance of PMS/Fe(II)/MoO$_2$ system compared with other

218 reported catalysts. Related to Figure **1**.

219

220

Valence state	IV	V+VI
Mo (before reaction)	26.2%	73.8%
Mo (after reaction)	25.7%	74.3%

221 **Table S2.** The variety of Mo valence distribution percentage before and after reaction.

222 Related to Figure **3**.

223

224

225

226

227

228

229

230

231

232

233

234

235

236

237

238
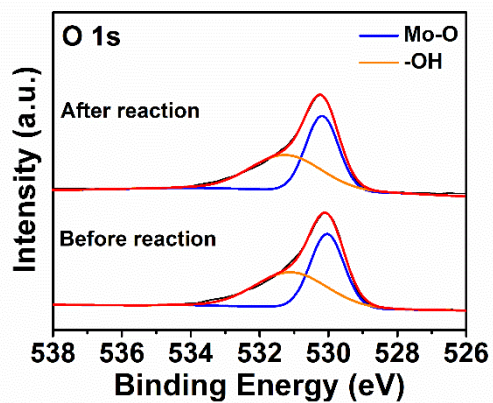
Figure S4. O1s spectra of MoO_2 before and after reaction in PMS/Fe(II)/MoO_2 system.

240 Related to Figure **3**.

241

242

243

244

245

246

247

248

249

250

251

252

253

254
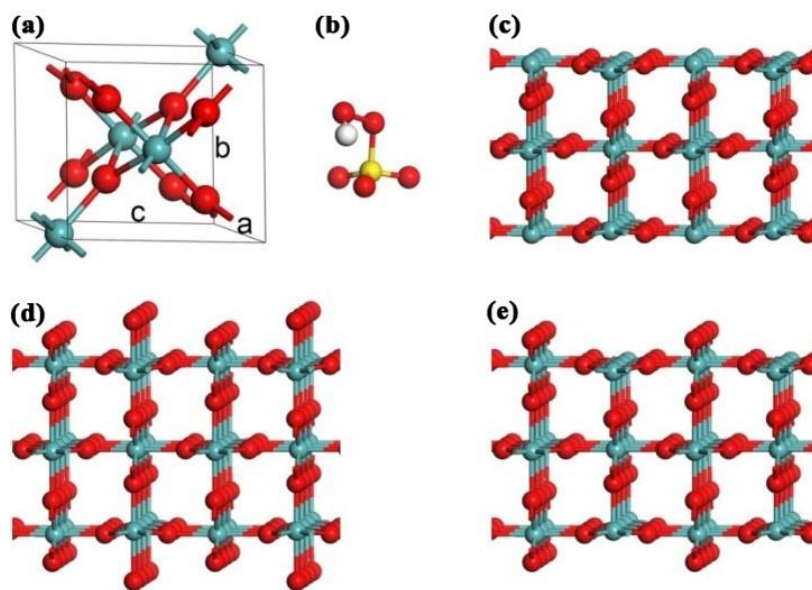
Figure S5. Optimized structure of MoO_2, PMS and three ideal terminations of (110) surface: (a) unite cell, (b) HSO_5^-, (c) the termination with exposed MoO active centers, (d) the termination with exposed O active centers, (e) the termination with exposed O' active centers. The yellow, red, olive, and white atoms are S, O, Mo, and H atoms, respectively. Related to Figure **4**.

260

261

262

263

264

265

266

267

268

269

270

271

272

Types	ΔE_{ads} (eV)	Δq (e)	l_{O-O} (Å)
Free HSO_5^- molecule	/	/	1.36
HSO_5^- on (110)	-2.06	0.62	1.40
HSO_5^- on Fe(II)-(110)	-3.17	0.75	1.48
$SO_4^{2-}+HO^{\cdot}$ on (110)	-1.68	0.69	/
$SO_4^{2-}+HO^{\cdot}$ on Fe(II)-(110)	-2.54	0.83	/

Table S3. The adsorption energy (ΔE_{ads}), the electron transfer between the molecule and MoO_2 (Δq), and the bond length (l_{O-O}) of $[SO_4\text{-}OH]^-$ in the different adsorption configurations. Related to Figure **4**.
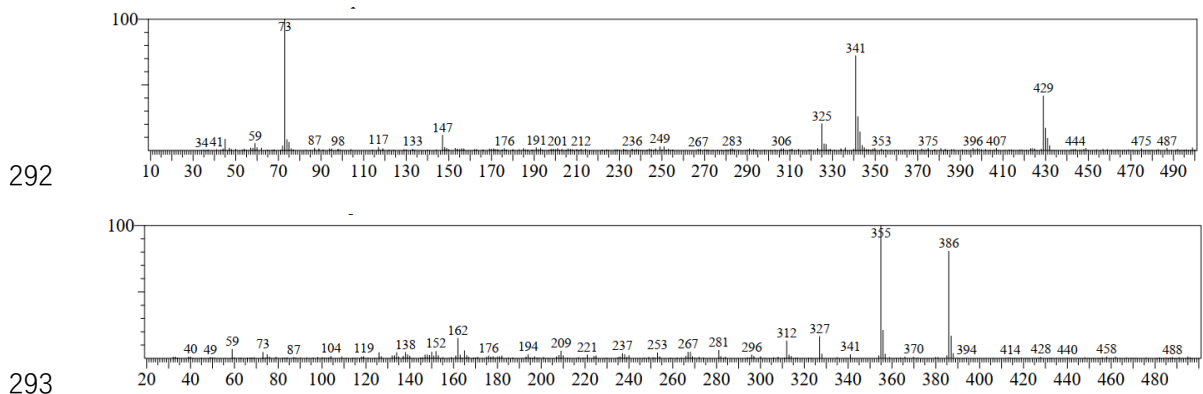
292

293

294 **Figure S6.** Mass spectrometry of phenol detected by GC-MS. Conditions: $[PMS]_0 =$

295 0.650 mM, $[Fe(II)]_0 = 0.036$ mM, $[MoO_2]_0 = 300$ mg/L, initial pH = 3.0, $[phenol]_0 =$

296 20 mg/L. Related to Figure **5**.

297

298

299

300

301

302

303

304

305

306

307

308

309

310

311

312

313

314

315

316
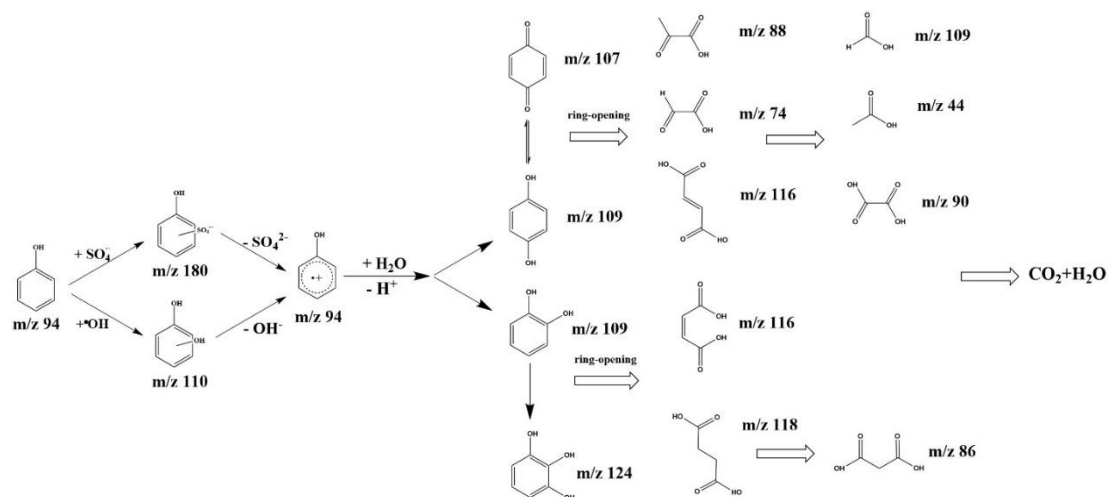
Scheme S1. Reaction pathway of phenol mineralization in the PMS/Fe(II)/MoO$_2$

system. Related to Figure **5**.

319

320

321

322

323

324

325

326

327

328

329

330

331

332

333

334

335

336

337
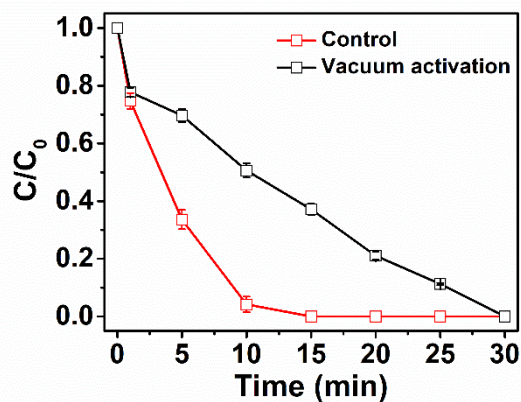
Figure S7. Recycling of MoO$_2$ after vacuum activation for PMS/Fe(II)/MoO$_2$ system.
General conditions: [PMS]$_0$ = 0.650 mM, [Fe(II)]$_0$ = 0.036 mM, [MoO$_2$]$_0$ = 300 mg/L,
initial pH = 3.0, [L-RhB]$_0$ = 20 mg/L. Error bars represent the standard deviation from
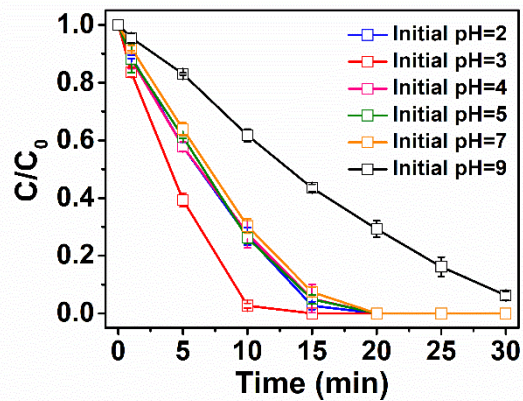at least duplicate experiments. Related to Figure **5**.

342

343

344

345

346

347

348

349

350

351

352

353

354

355

356

357

358

359
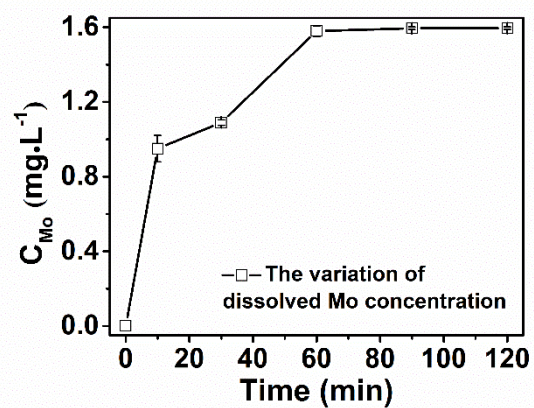
Figure S8. Dissolution of Mo ions in PMS/Fe(II)/ MoO_2 system. General conditions: $[PMS]_0 = 0.650$ mM, $[Fe(II)]_0 = 0.036$ mM, $[MoO_2]_0 = 300$ mg/L, initial pH = 3.0. Error bars represent the standard deviation from at least duplicate experiments. Related to Figure **5**.

383
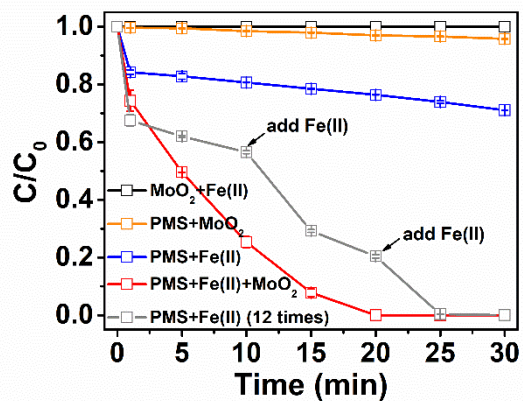
Figure S9. Scale up tests (1 L system). General conditions: $[PMS]_0 = 0.650$ mM, $[Fe(II)]_0 = 0.036$ mM, $[MoO_2]_0 = 300$ mg/L, initial pH = 3.0, $[L\text{-}RhB]_0 = 20$ mg/L. Error bars represent the standard deviation from at least duplicate experiments. Related to Figure **5**.
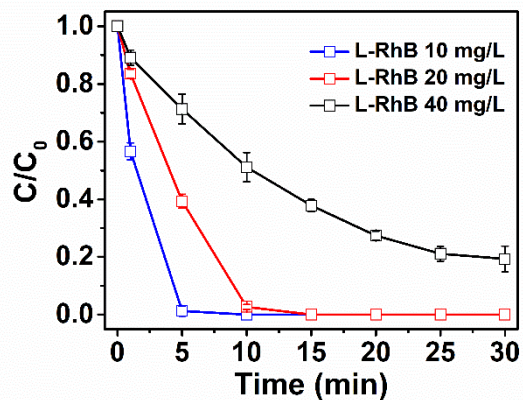
Figure S10. Degradation of different L-RhB concentration in PMS/Fe(III)/MoO$_2$ system. Conditions: $[PMS]_0 = 0.650$ mM, $[Fe(III)]_0 = 0.035$ mM, $[MoO_2]_0 = 300$ mg/L, initial pH = 3.0. Error bars represent the standard deviation from at least duplicate experiments. Related to Figure **5**.

428
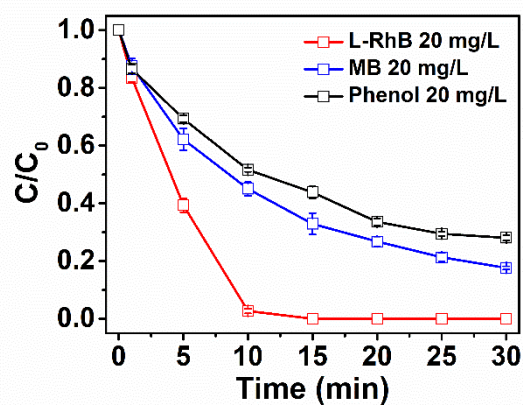
Figure S11. Degradation of different aromatic organic compounds in PMS/Fe(III)/MoO$_2$ system. Conditions: [PMS]$_0$ = 0.650 mM, [Fe(III)]$_0$ = 0.035 mM, [MoO$_2$]$_0$ = 300 mg/L, initial pH = 3.0, [aromatic organic compound]$_0$ = 20 mg/L. Error bars represent the standard deviation from at least duplicate experiments. Related to Figure **5**.
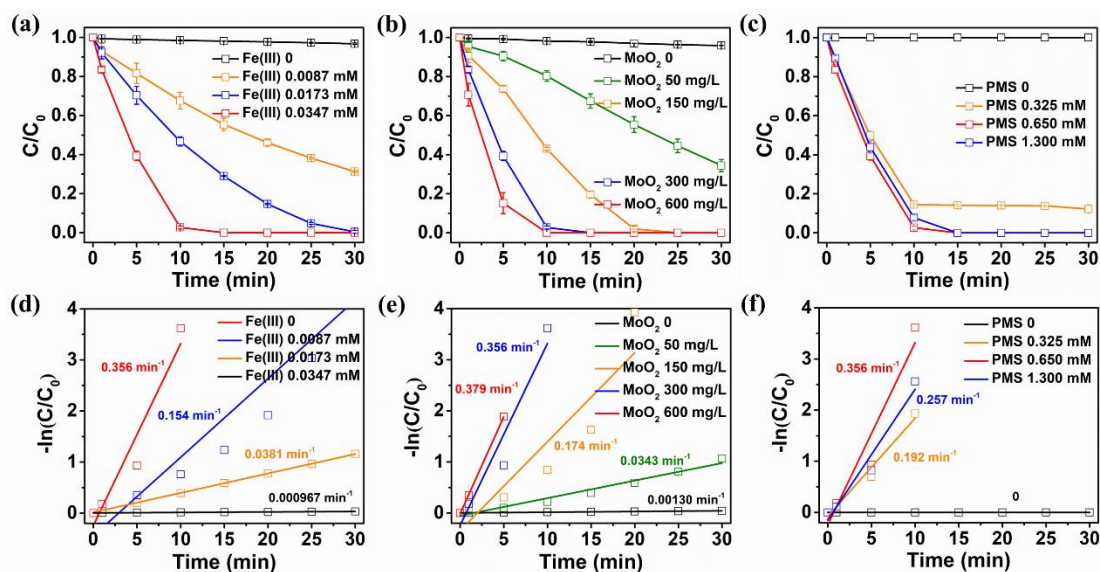
Figure S12. Effect of (a) Fe(III) concentration, (b) MoO_2 concentration, (c) PMS concentration on L-RhB degradation in $PMS/Fe(III)/MoO_2$ system; Pseudo-first-order kinetics of effect of (a) Fe(III), (b) MoO_2 and (c) PMS concentration in $PMS/Fe(II)/MoO_2$ system. Conditions: $[PMS]_0 = 0.650$ mM, $[Fe(III)]_0 = 0.035$ mM, $[MoO_2]_0 = 300$ mg/L, initial pH = 3.0, $[L-RhB]_0 = 20$ mg/L. Error bars represent the standard deviation from at least duplicate experiments. Related to Figure **5**.

Figure S13. Effect of initial pH in PMS/Fe(III)/MoO$_2$ system. Conditions: $[PMS]_0$ = 0.650 mM, $[Fe(III)]_0$ = 0.035 mM, $[MoO_2]_0$ = 300 mg/L, initial pH = 3.0, $[L\text{-}RhB]_0$ = 20 mg/L. Error bars represent the standard deviation from at least duplicate experiments. Related to Figure **5**.

472
473
474
475
476
477
478
479
480
481
482
483
484
485
486
487
488
489
490
491
492
493
494
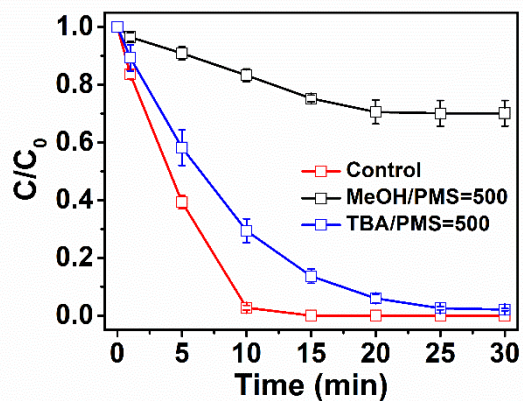
Figure S14. Inhibition effect of radical scavengers on L-RhB degradation in PMS/Fe(III)/MoO$_2$ system. Conditions: $[PMS]_0 = 0.650$ mM, $[Fe(III)]_0 = 0.035$ mM, $[MoO_2]_0 = 300$ mg/L, initial pH = 3.0, $[L\text{-}RhB]_0 = 20$ mg/L. Error bars represent the standard deviation from at least duplicate experiments. Related to Figure **5**.
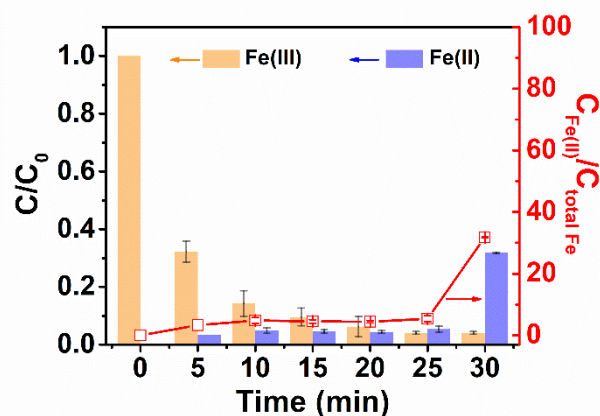
Figure S15. The variation of Fe(II) and Fe(III) concentrations in PMS/Fe(III)/MoO$_2$ system. General conditions: [PMS]$_0$ = 0.650 mM, [Fe(III)]$_0$ = 0.035 mM (total Fe), [MoO$_2$]$_0$ = 300 mg/L, initial pH = 3.0. Error bars represent the standard deviation from at least duplicate experiments. Related to Figure **5**.
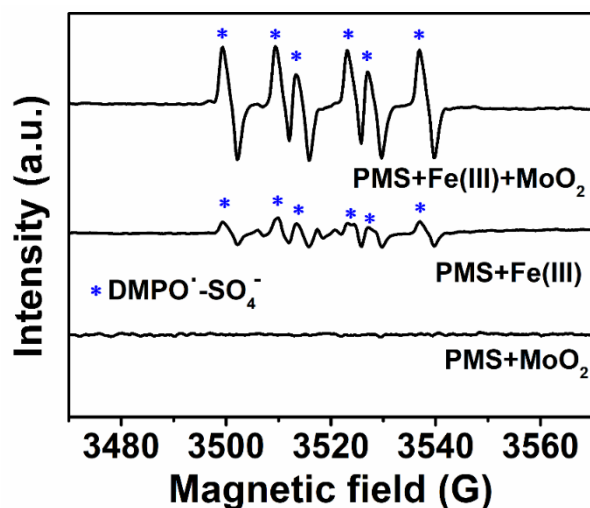
Figure S16. EPR spectra obtained from (i) PMS/MoO$_2$ system, (ii) PMS/Fe(III) system, and (iii) PMS/Fe(III)MoO$_2$ system with the existence of DMPO (* represents SO$_4^-$ adduct). Conditions: [PMS]$_0$ = 0.650 mM, [Fe(III)]$_0$ = 0.035 mM, [MoO$_2$]$_0$ = 300 mg/L, initial pH = 3.0. Related to Figure **5**.
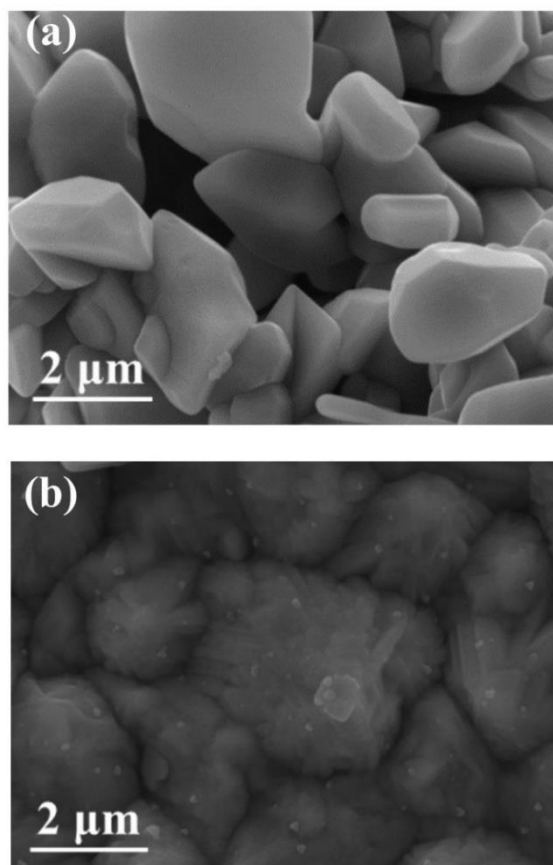
Figure S17. SEM images of MoO_2 (a) before and (b) after reaction in PMS/Fe(III)/MoO_2 system. Related to Figure **5**.
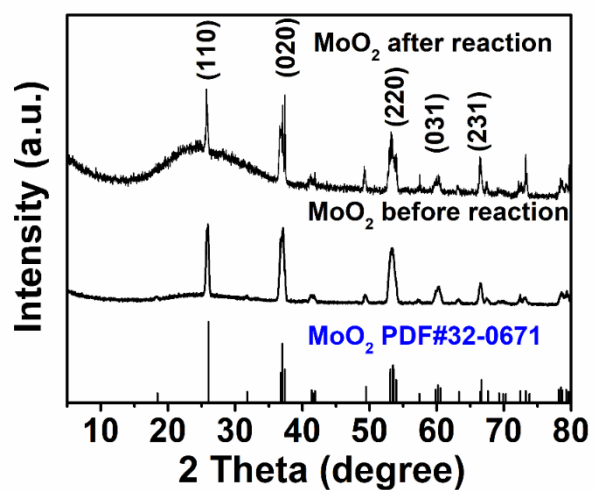
579

580 **Figure S18.** XRD patterns of MoO_2 before and after reaction in PMS/Fe(III)/MoO_2

581 system. Related to Figure **5**.

582

583
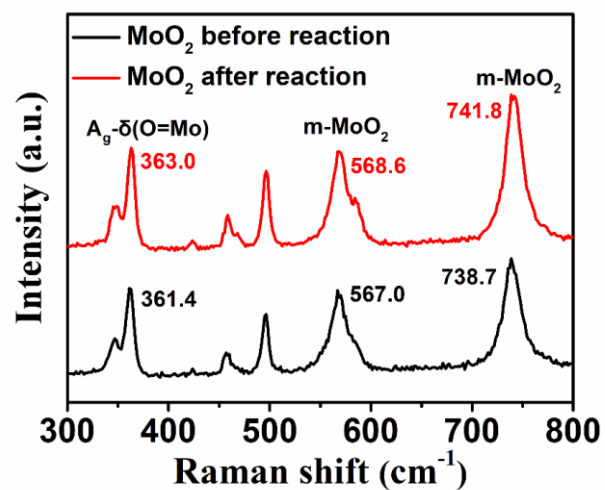
584

585

586

587

588

589

590

591

592

593

594

595

596

597

598

599

600

Figure S19. Raman spectra of MoO_2 before and after reaction in PMS/Fe(III)/MoO_2 system. Related to Figure **5**.
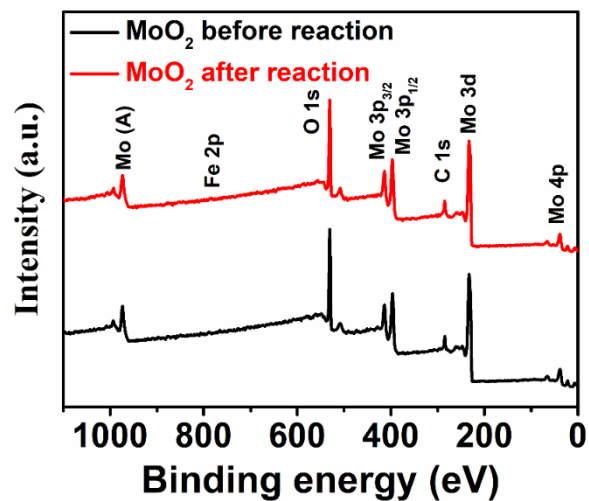
623

Figure S20. XPS survey spectra of MoO_2 before and after reaction in PMS/Fe(III)/MoO_2 system. Related to Figure **5**.

624
625
626
627
628
629
630
631
632
633
634
635
636
637
638
639
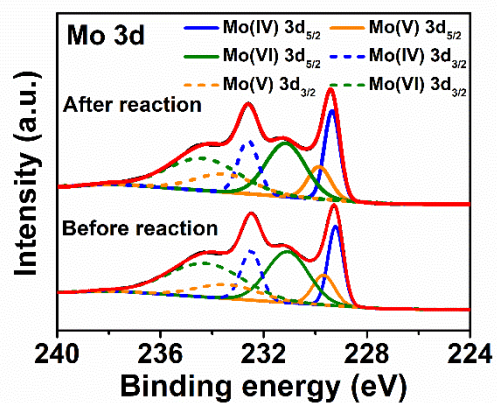640
641
642
643
644

645

646 **Figure S21.** Mo3d spectra of MoO_2 before and after reaction in $PMS/Fe(III)/MoO_2$

647 system. Related to Figure **5**.

648

649

650
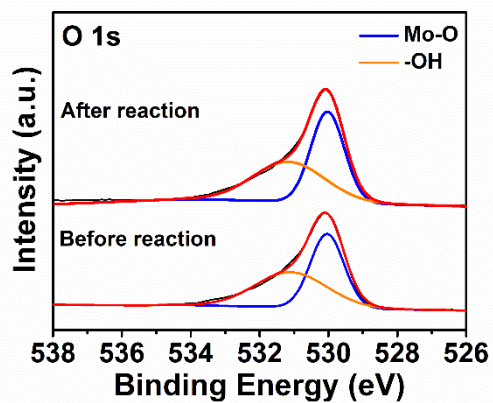
651

652

653

654

655

656

657

658

659

660

661

662

663

664

665

666

667

Figure S22. O1s spectra of MoO_2 before and after reaction in $PMS/Fe(III)/MoO_2$ system. Related to Figure **5**.

691 REFERENCES

692 Blum, V., Gehrke, R., Hanke, F., Havu, P., Havu, V., Ren, X., Reuter, K., and Scheffler, M. (2009).

693 Ab initio molecular simulations with numeric atom-centered orbitals. Computer Phys. Commun.

694 180, 2175-2196.

695 Gong, C., Chen, F., Yang, Q., Luo, K., Yao, F., Wang, S., Wang, X., Wu, J., Li, X., Wang, D. and

696 Zeng, G. (2017). Heterogeneous activation of peroxymonosulfate by Fe-Co layered doubled

697 hydroxide for efficient catalytic degradation of Rhoadmine B. Chem. Eng. J. 321, 222-232.

698 Kresse, G., and Joubert, D. (1999). From ultrasoft pseudopotentials to the projector augmented-

699 wave method. Phys. Rev. B 59, 1758-1775.

700 Li, H., Shan, C., and Pan, B. (2018a). Fe(III)-Doped g-C_3N_4 Mediated Peroxymonosulfate

701 Activation for Selective Degradation of Phenolic Compounds via High-Valent Iron-Oxo Species.

702 Environ. Sci. Technol. 52, 2197-2205.

703 Li, J., Xu, M., Yao, G. and Lai, B. (2018b). Enhancement of the degradation of atrazine through

704 $CoFe_2O_4$ activated peroxymonosulfate (PMS) process: Kinetic, degradation intermediates, and

705 toxicity evaluation. Chem. Eng. J. 348, 1012-1024.

706 Lin, K. Y. A., Chen, B. J., and Chen, C. K. (2016). Evaluating Prussian blue analogues

707 $MII_3[MIII(CN)_6]_2$ (MII = Co, Cu, Fe, Mn, Ni; MIII = Co, Fe) as activators for peroxymonosulfate

708 in water. RSC Adv. 6, 92923-92933.

709 Lu, J., Liu, Q., Xiong, Z., Xu, Z., Cai, Y., and Wang, Q. (2017). Activation of peroxymonosulfate

710 with magnetic and recyclable Fe_3O_4@C/$MnCo_2O_4$ nanocomposites for the decolorization of Acid

711 Orange II. J. Chem. Technol. Biot. 92, 1601-1612.

712 Monkhorst, H. J., and Pack, J. D. (1976). Special points for Brillouin-zone integrations. Phys. Rev.

713 B 13, 5188-5192.

714 Perdew, J. P., Burke, K., and Ernzerhof, M. (1996). Generalized gradient approximation made

715 simple. . Phys. Rev. Lett. 77, 3865-3868.

716 Perdew, J. P., Burke, K., and Ernzerhof, M. (2009). A grid-based Bader analysis algorithm without

717 lattice bias. J. Phys. Condens. Matt. 21, 084204.

718   Tkatchenko, A. and Scheffler, M. (2009). Accurate molecular van der Waals interactions from

719   ground-state electron density and free-atom reference data. Phys. Rev. Lett. 102, 073005.

720   Xu, Z., Lu, J., Liu, Q., Duan, L., Xu, A., Wang, Q., and Li, Y. (2015). Decolorization of Acid Orange

721   II dye by peroxymonosulfate activated with magnetic Fe_3O_4@C/Co nanocomposites. RSC Adv. 5,

722   76862-76874.

723   Yang, B., Tian, Z., Wang, B., Sun, Z., Zhang, L., Guo, Y., Li, H. and Yan, S. (2015). Facile synthesis

724   of Fe_3O_4/hierarchical-Mn_3O_4/graphene oxide as a synergistic catalyst for activation of

725   peroxymonosulfate for degradation of organic pollutants. RSC Adv. 5, 20674-20683.

726   Yao, Y., Chen, H., Lian, C., Wei, F., Zhang, D., Wu, G., Chen, B. and Wang, S. (2016). Fe, Co, Ni

727   nanocrystals encapsulated in nitrogen-doped carbon nanotubes as Fenton-like catalysts for organic

728   pollutant removal. J. Hazard. Mater. 314, 129-139.

729   Zhang, S., Fan, Q., Gao, H., Huang, Y., Liu, X., Li, J., Xu, X. and Wang, X. (2016). Formation of

730   Fe_3O_4@MnO_2 ball-in-ball hollow spheres as a high performance catalyst with enhanced catalytic

731   performances. J. Mater. Chem. A 4, 1414-1422.

732   Zou, J., Ma, J., Chen, L., Li, X., Guan, Y., Xie, P. and Pan, C. (2013). Rapid acceleration of ferrous

733   iron/peroxymonosulfate oxidation of organic pollutants by promoting Fe(III)/Fe(II) cycle with

734   hydroxylamine. Environ. Sci. Technol. 47, 11685-91.

735